# Interplay of orbital and spin magnetization in trigonal tellurium

Zhenqi Hua[1, 2, *], Chang Niu[3, 4, *], Sandeep Joy[1, 2, *], Pukun Tan[3, 4], Gang Shi[1], Haoyang Liu[1], Jiaxing Guo[1], David Graf[2], Peide Ye[3, 4], Cyprian Lewandowski[1, 2], and Peng Xiong[1, †]

1. *Department of Physics, Florida State University, Tallahassee, FL 32306*
2. *National High Magnetic Field Laboratory, Tallahassee, FL 32310*
3. *Elmore Family School of Electrical and Computer Engineering, Purdue University, West Lafayette, Indiana 47907*
4. *Birck Nanotechnology Center, Purdue University, West Lafayette, Indiana 47907*

[*] Z.H, C.N., and S.J. contributed equally to this work

[†] pxiong@fsu.edu

## Abstract

Orbital effects, despite their fundamental significance and potential to engender novel physical phenomena and enable new applications, have long been underexplored compared to their spin counterparts. Recently, surging interest in the orbital degree of freedom has led to the discovery of a plethora of orbital-related effects, underscoring the need for a deeper understanding of their roles in quantum materials. Here, we report first experimental signatures of orbital magnetization in trigonal Tellurium, an elemental semiconductor with a unique helical crystal structure that serves as a natural platform for investigating orbital effects. Detailed angular dependent linear and nonlinear magnetotransport measurements, supported by theoretical Boltzmann transport analysis, reveal the coexistence of current-induced spin polarization and orbital magnetization. By disentangling the interplay between spin and orbital degrees of freedom, this work establishes a general framework for understanding orbital magnetization in chiral crystals and beyond, paving the way for its utilization in orbitronics and spintronics.

## Introduction

The orbital degree of freedom, a fundamental component of electron angular momentum, has long been overshadowed by its spin counterpart. However, recent theoretical and experimental advancements have reignited interest in orbital effects, revealing their profound influence on material properties. Phenomena such as the orbital Hall effect[1–3], intrinsic planar Hall effect[4], chiral orbital current[5], and orbital Chern states[6] have demonstrated the rich physics arising from orbital dynamics. Moreover, Berry phase physics has established that orbital angular momentum and magnetization are intrinsic properties of electronic wavefunctions in solids[7], providing a unified framework for understanding these effects.

Despite these advancements, clear observation of orbital effects has been hindered by the inherent entanglement between the orbital and spin degrees of freedom in materials with spin-orbit coupling (SOC)[2], thus largely limited to light-element materials. Moreover, it has been shown that in several previously studied systems where the observations were attributed solely to spins, there are in fact substantial contributions from orbitals[8–10]. While orbital angular momentum can directly impact material properties through interaction with magnetic fields via Zeeman-like coupling even without SOC[4], the precise mechanisms by which orbital magnetization contribute to magnetotransport in the presence of SOC should be carefully elucidated.

Symmetry and its breaking play a crucial role in condensed matter physics. Various spatial and time-reversal symmetries have enabled the discovery of new topological phases through protected features in electronic band structures[11–14]. Conversely, symmetry breaking often leads to novel emergent phenomena[15–17], opening new frontiers in quantum materials research. One notable example is structural chirality, a distinct form of spatial inversion symmetry breaking, which has emerged as a focal point of studies[18,19]. In chiral materials, two distinct charge-spin conversion effects have been widely studied: the collinear Rashba-Edelstein effect in conducting chiral crystals[20–26] and chirality-induced spin selectivity in chiral molecules[27–29]. In both cases, there are tantalizing clues that orbital polarization plays essential roles[30–33]. However, despite significant progress in understanding spin polarization in chiral materials, definitive experimental observation of orbital magnetization arising from structural chirality remains elusive. Prior studies in chiral crystals have also been limited to current and field configurations aligned with the helical axis, focusing primarily on spin polarization along the helical axis.

Here, we report first experimental signatures of orbital magnetization in Tellurium (Te) from a comprehensive set of magnetotransport measurements on pre-patterned ‘L’-bar devices. The results reveal distinct features of orbital magnetization that coexist with spin polarization. Notably, we observed an unexpected orbital magnetization component perpendicular to the helical chains. Moreover, the relative contributions of the spin and orbital effects could be tuned by electrostatic gating, enabling precise control and detailed study of their interplay with varying chemical potential. Our theoretical framework elucidates a general relationship between the electronic structure of Te and its spin polarization and orbital magnetization. Within the Boltzmann transport framework, we are able to explain the experimental trends as an interplay and competition between the spin polarization and orbital (perpendicular to the axis of the helix) magnetization. We argue that the finite magnetization perpendicular to the helical axis is a natural consequence of the helical structure of Te. Taking together, our experimental and theoretical findings help advance the fundamental understanding of orbital dynamics in chiral materials and highlight the ubiquity of orbital effects.

## Magnetotransport signatures of orbital magnetization

Te crystals exhibit $D_3$ symmetry, comprising helical chains of covalently bonded atoms, arranged into a hexagonal close-packed structure via inter-chain van der Waals interactions. The left-handed crystal structure (space group $P3_221$) is illustrated in Fig. 1a. The 'L'-bar device structure (Fig. 1b), with two arms aligned along different crystalline axes, enables thorough examination of all possible configurations of current and magnetic field orientations relative to the chiral crystal axis within a single device. Single-crystal Te flakes are synthesized through hydrothermal growth[34], and then transferred onto $Si^{++}/SiO_2$ wafers. A flake is identified and patterned into an 'L'-bar, followed by another lithography step to define the metal electrodes. The fundamental ($\omega$) and second harmonic ($2\omega$) voltages are measured in both longitudinal and transverse configurations. The sample can be rotated *in situ* over 360° in two orthogonal directions, allowing for measurements in all in-plane (red arrow) and out-of-plane (green arrow) orientations. This setup enables the determination of eight components of longitudinal and transverse resistances: $R_{zz}^{\omega}$, $R_{xx}^{\omega}$, $R_{xz}^{\omega}$, $R_{zx}^{\omega}$, $R_{zz}^{2\omega}$, $R_{xx}^{2\omega}$, $R_{xz}^{2\omega}$, and $R_{zx}^{2\omega}$ - In the following analysis, we focus on the four longitudinal components. In addition, using the degenerately doped Si as a backgate, the above measurements can be performed with the Fermi level positioned near (green contours) and away (blue contour) from the characteristic camelback-like features at the top of the valence band, see Fig. 1c. As will be demonstrated below, this tunability allows us to control the extent of competition between the spin and orbital components. Current induced spin polarization in Te due to the collinear REE is illustrated in Fig. 1d. For the orbital contribution, our model predicts orbital magnetization with two orthogonal components, $\boldsymbol{M}_{orb,z}$ along and $\boldsymbol{M}_{orb,x}$ perpendicular to the helical axis (Fig. 1e). Unlike an ideal solenoid, the distorted helix crystal structure of Te (with lattice constant $c > a$ ) leads to a significant orbital moment in $x$-direction.

The linear-response resistivities along $c$- and $a$-axis exhibit similar magnitudes and temperature dependences, regardless of whether the Fermi level lies within the bandgap or inside the valence band. Hall measurements also reveal nearly identical carrier densities along these two axes (Extended Data Fig. 1 and reference therein[35–37]). These common properties ensure valid direct comparison of linear and nonlinear magnetotransport stemming from spin polarization and orbital magnetization along the two axes, which rely on values of $R_{zz}^{\omega(2\omega)}$ and $R_{xx}^{\omega(2\omega)}$. The linear-response magnetoresistance (MR) was calculated from the symmetric component of fundamental (first harmonic) voltage with varying magnetic field. For the nonlinear contribution, the quantity $\delta^{NL} = \frac{2R^{2\omega}}{R^{\omega}}$ is employed; the antisymmetric component of which with respect to the magnetic field excludes any contributions from trivial MR, nonlinear resistivity, and ordinary Hall effect due to misalignment (see Methods).

Figure 2a shows the angular dependence of the linear MR along the helical axis ($R_{zz}^{\omega}$) under an in-plane magnetic field ranging from 2 T to 12 T. The data was obtained from device D1 at the natural doping level of the as-grown sample. The zero-field $R_{zz}^{\omega}$ is represented by the horizontal green dotted line for reference. The linear MR exhibits 180° periodicity with respect to the magnetic field, with negative MR observed when the field aligns with the helical axis. The resistance minima, marked by the vertical gray dashed lines, reveals an experimental misalignment of approximately 5° with respect to the helical axis. However, this misalignment is systematic and independent of the magnetic field, thus has no impact on the subsequent discussions. We note that there is no discernible difference between the resistances with the magnetic field parallel ($\phi \approx 360°$) or antiparallel ($\phi \approx 180°$) to the current direction.

The angular dependence of $\delta_{zz}^{NL}$ is shown in Fig. 2b, exhibiting a 360°-periodicity with a magnitude that increases monotonically but nonlinearly with the magnetic field. Notably, at low magnetic fields, the angular positions of the maxima (minima) deviate significantly from 360° (180°) expected from current-induced collinear spin polarization. As the field strength increases, the maxima (minima) approaches 360° (180°) and the angular shift from the 360° (180°) orientation diminishes toward zero. The angular shift at low fields is more apparent, as shown in Fig. 2g, which presents the quantity normalized by the magnetic field, $\frac{\delta_{zz}^{NL}}{\mu_0 H}$; an angular shift of approximately 45° at 2 T is evident. For the $a$-axis, Fig. 2c presents the angular dependence of $\delta_{xx}^{NL}$, along with its normalized data shown in Fig. 2h. Conventionally, spin orientation along $a$-axis is expected to be invariant under momentum inversion due to the preservation of mirror symmetry, implying zero spin polarization. However, trigonal wrapping[38] in the Te band structure breaks the inversion symmetry along $a$-axis, potentially contributing to nonlinear magnetotransport. Interestingly, at 2 T, $\delta_{xx}^{NL}$ exhibits wide plateaus centered at 360° and 180°, with a normalized magnitude comparable to $\delta_{zz}^{NL}$. As the magnetic field strength increases, additional side peaks emerge, and the normalized magnitude decreases significantly, making $\delta_{xx}^{NL}$ much smaller than $\delta_{zz}^{NL}$ at high fields. Although pronounced features consistent with collinear current-induced spin polarization are observed in D1, the angular shift in $\delta_{zz}^{NL}$ at small fields and complex magnetic field dependence of $\delta_{xx}^{NL}$ cannot be explained by spin polarization alone. The comparable magnitudes of $\delta_{zz}^{NL}$ and $\delta_{xx}^{NL}$ at 2T strongly suggest an additional underlying contribution to $\delta^{NL}$.

Figures 2d-f present the angular dependence of $R_{zz}^{\omega}$, $\delta_{zz}^{NL}$, and $\delta_{xx}^{NL}$ measured on device D2 without an applied gate voltage under in-plane rotation of the magnetic field at different strengths. These results exhibit contrasting behavior compared to D1. Notably, the angular position of $R_{zz}^{\omega}$ minima shifted from $\phi \approx 180°$ (or $\phi \approx 360°$) and increased approximately linearly with the magnetic field, as indicated by the gray dashed lines. Note that this field-enhanced angular shift is absent in Fig. 2a. Similarly, field normalized $\delta_{zz}^{NL}$ and $\delta_{xx}^{NL}$ in Figs. 2i and 2j, respectively, also display linear field dependence, with their angular shifts increasing as the field strength rises (indicated by gray dashed lines). However, the magnitude and shifted angle of $\delta_{zz}^{NL}$ are significantly greater than those of $\delta_{xx}^{NL}$, consistent with the smaller angular shift in $R_{xx}^{\omega}$ (Extended Data Fig. 2). Specifically, the onset of the $\delta_{zz}^{NL}$ angular shift is approximately 20° left of 180° (or 360°), whereas $\delta_{xx}^{NL}$ exhibits only a slight deviation from these angles. The observations from D2 clearly extend beyond the framework of collinear spin polarization, suggesting the presence of a polarization/magnetization component perpendicular to the helical axis that competes with the collinear spin polarization. This component couples to the external magnetic field linearly, becoming more pronounced as the field increases and leads to the enhanced angular shift away from the helical chain direction. The current dependences of $R^{\omega}$ and $\delta^{NL}$ in D1 and D2 are shown in Extended Data Figs. 3 and 4, respectively, which further indicate the existence of higher-order terms (see Methods).

The contrasting behaviors between D1 and D2 can be attributed to the different SOC strengths in the two samples due to the different locations of the Fermi level at different native doping levels as grown. SOC in Te exhibits significant tunability via electrostatic gating[39], which is confirmed in our samples by a transition from weak localization (WL) to weak anti-localization (WAL) (Extended Data Fig. 5). A similar transition is observed as the Fermi level shifts from the valence band edge (in D2) to deep in the valence band (in D1) (Extended Data Fig. 6). This transition signifies a weaker SOC near the camelback and stronger SOC deeper in the valence band. Resistivity versus temperature and perpendicular field MR measurements on D1 and D2 are shown in Extended Data Fig. 6. The MR of D1 shows a flat response near zero field, indicating the SOC strength lies in the transition regime from WL to WAL, which indicates that without any applied gate voltage, the Fermi level of D1 lies inside the valence band. The SOC in D1 is strong enough to induce pronounced collinear spin polarization due to spin-momentum locking, as evidenced by Fig. 2b at high fields. In contrast, D2 exhibits pure WL MR, indicating weak SOC. Furthermore, since the Fermi level of D2 is close to the band edge, the absolute value of the momentum is reduced, making spin-momentum locking less effective which minimizes contributions from spin polarization.

Based on these observations, we argue that the observed $\delta_{zz}^{NL}$ and $\delta_{xx}^{NL}$ in D2 are signatures of pronounced orbital magnetization. We emphasize that although a magnetic field along the helical axis may induce energy dispersion shifts[40], they would not lead to a shifted angular dependence in either linear or nonlinear MR (Fig. 4a).

## Gate tunability

To determine the evolution of these phenomena with the Fermi level, we employed electrostatic gating to modulate the electronic properties of D2, covering a wide range of chemical potential below the valence band maximum. Figure 3a presents the normalized $R_{zz}^{\omega}$ under different gate voltages where a higher negative voltage corresponds to a chemical potential residing deeper inside the valence band. Notably, the angular shift of the resistance minima vanishes at sufficiently large negative gate voltages, closely aligning with the transition from WL to WAL, i.e. strengthening of the spin polarization contribution as the magnitude of the negative gate voltage increases (Extended Data Fig. 6). At $V_{gate}$ = -6 V, where the hole density of D2 is tuned close to that of D1 without gating, the angular dependence of $R_{zz}^{\omega}$ closely resembles the behavior observed in Fig. 2a. Furthermore, measurements at this gate voltage yielded results essentially identical to those of D1, demonstrating a remarkable degree of consistency between samples of quite different native doping levels, and the high reproducibility and robustness of the observations (Extended Data Fig. 7). Mapping of $\delta_{zz}^{NL}$ with the gate voltage (Fig. 3b) illustrates a clear transition between the orbital effects dominated and spin polarization dominated regions, marked by the vanishing angular shift from the 180° (antiparallel) and 360° (parallel) field orientation (indicated by the white dashed lines). The gate voltage mapping of $\delta_{xx}^{NL}$ is shown in Extended Data Fig. 8, which demonstrates the same transition. The enhancement of SOC deeper in the valence band induces stronger collinear spin polarization, while the pure orbital effect is quenched due to enhanced SOC as the chemical potential moves away from the band edge, resulting in the maxima (minima) of $\delta_{xx}^{NL}$ appear at $\phi \approx 360°$ ($\phi \approx 180°$). It is interesting to note that, near the band edge, the magnitude of $\delta_{zz}^{NL}$ exceeds that inside the valence band (due to spin polarization) and continues to increase as the gate voltage increases (Extended Data Fig. 9). This suggests that the orbital effects lead to greater nonlinear MR than spin alone, further highlighting that additional spin polarization may have originated from the conversion of orbital angular momentum in the presence of SOC. These findings highlight the high tunability of the interplay between orbital and spin effects, broadening potential applications in orbitronics and spintronics.

To conclude the experimental characterization of the samples, we also examined the case of an out-of-plane magnetic field, where nonlinear MR has been observed in both bulk and 2D Te[26,41]. Figures 3c and 3d present the angular dependence of $\delta_{zz}^{NL}$ measured on D2 under different gate voltages and out-of-plane rotation of the applied field. The $\delta^{NL}$ in the presence of an out-of-plane magnetic field is consistently captured, with a magnitude comparable to that seen in in-plane field rotation. A hump at $\theta = 0°$ ($\phi = 270°$) and a dip at $\theta = 180°$ ($\phi = 90°$) are observed, consistent with nonzero $\delta^{NL}$ at those positions due to angular shift under in-plane rotation at $V_{gate} = 0$ V. Notably, as the angular shift vanishes when the Fermi level is tuned to spin polarization dominant region (deep in the valence band), the curve reverts to a simple sin($\theta$)-like behavior with respect to out-of-plane magnetic field, aligning with previous observations in Te[26,41]. Taken together, our gate tuning measurements significantly extend the understanding of the magnetotransport properties in this material

## Discussions

To help interpret the experimental results, we perform a semiclassical Boltzmann transport calculation to extract both the linear and nonlinear conductivities. Full details of the calculation are provided in the Supplemental Information and References therein[42–61]. Within linear response to magnetic field, our model takes the general form:

$$\varepsilon(\vec{q}) = \varepsilon_0(\vec{q}) - \mu_B B_{\parallel} \cos(\phi)\,(s_z + m_z) - \mu_B B_{\parallel} \sin(\phi)\,(s_x + m_x)$$

Here, $\varepsilon_0\,(\vec{q})$ denotes the band dispersion without a magnetic field, $\mu_B$ is the Bohr magneton, and the latter terms represent the Zeeman coupling to an in-plane magnetic field of magnitude $B$

oriented along ($\sin(\phi)$, 0, $\cos(\phi)$). Total magnetization thus includes both orbital ($\boldsymbol{m}$) and spin ($\boldsymbol{s}$) contributions which we define below.

In Figs. 4a-f, we present results for three different model scenarios that help us substantiate proposed experimental interpretation of competing spin and orbital polarizations. First, in Figs. 4a, d, we demonstrate that spin texture alone, i.e. the collinear spin model, is insufficient to account for the experimentally observed trends – the resistance curves' maxima/minima are rigidly locked along the colinear and anti-colinear directions. Second, we conduct a symmetry analysis of orbital magnetization and find that only an orbital magnetization component that is odd in $q_z$ can explain the experimentally observed shift in the minima of the resistance (Figs. 4b and 4e). Here, we use a parameter $\alpha$ as a tuning parameter, such that $\alpha = 0$ corresponds to a situation in which orbital magnetization is absent and $\alpha = 1$ corresponds to purely orbital magnetization with no spin magnetization. Physically, if one views the helical chains as one-dimensional spirals, it is natural to expect components of orbital magnetization along all three spatial directions (Fig. 1e). This conclusion is further supported by a toy model of a helical chain with three atoms per unit cell, which validates the symmetry-based argument (Figs. 4c and 4f). In the supplementary materials we review existing models of the band structure of Te and find that they either yield no orbital magnetization or the magnetization lacks the $q_z$ dependence on the crystal momentum and yield just the collinear result.

Taken together with experimental results, the theoretical calculations of Fig. 4 consistently support the interpretation of coexisting current-induced spin polarization and orbital magnetization, with orbital contribution being most pronounced near the valence band edge where SOC is weak. In chiral materials such as Te, orbital magnetization differs from spin polarization by having two orthogonal components, $\boldsymbol{M}_{orb,z}$ along helical axis and $\boldsymbol{M}_{orb,x}$ perpendicular to it, as illustrated in Fig. 1e and naturally arising in a simple helical tight-binding model. Deeper in the valence band, where spin effects dominate, current-induced spin polarization $\Delta\boldsymbol{S}$ (Fig. 1d) overwhelms $\boldsymbol{M}_{orb}$. In this regime, the magnetic field both (1) couples to $\Delta\boldsymbol{S}$ to induce $\delta^{NL}$, and (2) amplifying $\Delta\boldsymbol{S}$ by creating an imbalance in spin occupation states. The angular shift at low magnetic fields (Fig. 2b) reflects the mixing of $\Delta\boldsymbol{S}$ and $\boldsymbol{M}_{orb,x}$; as the magnetic field increases, $\boldsymbol{M}_{orb,x}$ becomes negligible comparing to $\Delta\boldsymbol{S}$, resulting in collinear maxima and minima. Near the band edge, where orbital magnetization dominates, the ratio between its components along and perpendicular to the helical axis evolves with increasing magnetic field (Fig. 2e) while remaining constant for different current bias (Extended Data Fig. 4b).

## Conclusion

A comprehensive set of linear- and nonlinear response magnetotransport measurements covering all relative orientations of applied magnetic field and bias current with respect to the helical crystalline axis was conducted on trigonal Te, a chiral material with a distinct helical crystal structure. The results revealed experimental evidence naturally interpreted as signatures of orbital magnetization, specifically, the coexistence of current-induced spin polarization and two orthogonal components of orbital magnetization. By disentangling their contributions to magnetotransport via electrostatic gating, we identify distinct linear- and nonlinear-response behaviors that align with theoretical predictions. These findings provide deeper insight into the interplay between spin and orbital degrees of freedom in chiral materials. Our results establish Te as an excellent platform for studying the interplay of orbital magnetization with rich spin structures.

## Acknowledgements

We acknowledge fruitful discussions with O. Vafek, D. Chichinadze, J. Padayasi, and Z. Lu. We thank L. Golub, D. Pesin, and M. Sakano for valuable discussions over email. P.X. is supported by NSF grant no. DMR-1905843 and DMR-2325147. S.J. acknowledges support from Florida State University through the Quantum Postdoctoral Fellowship and the National High Magnetic Field Laboratory. C.L. was supported by start-up funds from Florida State University and the National High Magnetic Field Laboratory. The National High Magnetic Field Laboratory is supported by the National Science Foundation through NSF/DMR-2128556 and the State of Florida.

## Author contributions

P.X. supervised the project. Z.H. and D.G. performed the magnetotransport measurement. C.N. and P.T. grew Te single crystals. Z.H., G.S., H.L., and J.G. fabricated the devices. S.J. and C.L. performed the calculations. All authors discussed the results and wrote the paper.

## Competing interests

The authors declare no competing interests.

## Data availability

The data that support this study are reported in the manuscript and Supplementary Information. Source data and other data are available from the corresponding authors on request.

**Reference:**

1. Choi, Y. G. *et al.* Observation of the orbital Hall effect in a light metal Ti. *Nature* **619**, 52–56 (2023).
2. Go, D., Jo, D., Kim, C. & Lee, H. W. Intrinsic Spin and Orbital Hall Effects from Orbital Texture. *Phys Rev Lett* **121**, (2018).
3. Wang, P. *et al.* Inverse orbital Hall effect and orbitronic terahertz emission observed in the materials with weak spin-orbit coupling. *NPJ Quantum Mater* **8**, (2023).
4. Wang, H. *et al.* Orbital Origin of the Intrinsic Planar Hall Effect. *Phys Rev Lett* **132**, (2024).
5. Zhang, Y. *et al.* Control of chiral orbital currents in a colossal magnetoresistance material. *Nature* **611**, 467–472 (2022).
6. Polshyn, H. *et al.* Electrical switching of magnetic order in an orbital Chern insulator. *Nature* **588**, 66–70 (2020).
7. Xiao, D., Chang, M. C. & Niu, Q. Berry phase effects on electronic properties. *Rev Mod Phys* **82**, 1959–2007 (2010).
8. El Hamdi, A. *et al.* Observation of the orbital inverse Rashba–Edelstein effect. *Nat Phys* **19**, 1855–1860 (2023).
9. Hayashi, H., Go, D., Haku, S., Mokrousov, Y. & Ando, K. Observation of orbital pumping. *Nat Electron* **7**, 646–652 (2024).
10. Lee, D. *et al.* Orbital torque in magnetic bilayers. *Nat Commun* **12**, (2021).
11. Hasan, M. Z. & Kane, C. L. Colloquium: Topological insulators. *Rev Mod Phys* **82**, 3045–3067 (2010).
12. Qi, X. L. & Zhang, S. C. Topological insulators and superconductors. *Rev Mod Phys* **83**, (2011).
13. Armitage, N. P., Mele, E. J. & Vishwanath, A. Weyl and Dirac semimetals in three-dimensional solids. *Rev Mod Phys* **90**, (2018).
14. Yan, B. & Felser, C. The Annual Review of Condensed Matter Physics is Downloaded from www.annualreviews.org. *Annu. Rev. Condens. Matter Phys* **8**, 9 (2025).
15. McGreevy, J. Generalized Symmetries in Condensed Matter. *Annu Rev Condens Matter Phys* **14**, 57–82 (2023).
16. Fischer, M. H., Sigrist, M., Agterberg, D. F. & Yanase, Y. Superconductivity and Local Inversion-Symmetry Breaking. *Annu Rev Condens Matter Phys* **14**, 153–172 (2023).

17. Du, L. *et al.* Engineering symmetry breaking in 2D layered materials. *Nature Reviews Physics* vol. 3 193–206 Preprint at https://doi.org/10.1038/s42254-020-00276-0 (2021).

18. Sanchez, D. S. *et al.* Topological chiral crystals with helicoid-arc quantum states. *Nature* **567**, 500–505 (2019).

19. Chang, G. *et al.* Topological quantum properties of chiral crystals. *Nat Mater* **17**, 978–985 (2018).

20. Tenzin, K. *et al.* Collinear Rashba-Edelstein effect in nonmagnetic chiral materials. *Phys Rev B* **108**, (2023).

21. Sakano, M. *et al.* Radial Spin Texture in Elemental Tellurium with Chiral Crystal Structure. *Phys Rev Lett* **124**, (2020).

22. Gatti, G. *et al.* Radial Spin Texture of the Weyl Fermions in Chiral Tellurium. *Phys Rev Lett* **125**, (2020).

23. Roy, A. *et al.* Long-range current-induced spin accumulation in chiral crystals. *NPJ Comput Mater* **8**, (2022).

24. Hirayama, M., Okugawa, R., Ishibashi, S., Murakami, S. & Miyake, T. Weyl Node and Spin Texture in Trigonal Tellurium and Selenium. *Phys Rev Lett* **114**, (2015).

25. Calavalle, F. *et al.* Gate-tuneable and chirality-dependent charge-to-spin conversion in tellurium nanowires. *Nat Mater* **21**, 526–532 (2022).

26. Niu, C. *et al.* Tunable Chirality-Dependent Nonlinear Electrical Responses in 2D Tellurium. *Nano Lett* **23**, 8445–8453 (2023).

27. Göhler, B. *et al.* Spin Selectivity in Electron Transmission Through Self-Assembled Monolayers of Double-Stranded DNA. *Science (1979)* **331**, 894–897 (2011).

28. Waldeck, D. H., Naaman, R. & Paltiel, Y. The spin selectivity effect in chiral materials. *APL Mater* **9**, 040902 (2021).

29. Liu, T. *et al.* Linear and nonlinear two-terminal spin-valve effect from chirality-induced spin selectivity. *ACS Nano* **14**, 15983–15991 (2020).

30. Yoda, T., Yokoyama, T. & Murakami, S. Current-induced orbital and spin magnetizations in crystals with helical structure. *Sci Rep* **5**, (2015).

31. Yoda, T., Yokoyama, T. & Murakami, S. Orbital Edelstein Effect as a Condensed-Matter Analog of Solenoids. *Nano Lett* **18**, 916–920 (2018).

32. Liu, Y., Xiao, J., Koo, J. & Yan, B. Chirality-driven topological electronic structure of DNA-like materials. *Nat Mater* **20**, 638–644 (2021).

33. Adhikari, Y. *et al.* Interplay of structural chirality, electron spin and topological orbital in chiral molecular spin valves. *Nat Commun* **14**, (2023).

34. Wang, Y. *et al.* Field-effect transistors made from solution-grown two-dimensional tellurene. *Nat Electron* **1**, 228–236 (2018).

35. Qiu, G. *et al.* Quantum Hall effect of Weyl fermions in n-type semiconducting tellurene. *Nat Nanotechnol* **15**, 585–591 (2020).

36. Suárez-Rodríguez, M. *et al.* Odd Nonlinear Conductivity under Spatial Inversion in Chiral Tellurium. *Phys Rev Lett* **132**, (2024).

37. Chichinadze, D. V. *et al.* Observation of giant nonlinear Hall conductivity in Bernal bilayer graphene. (2024).

38. Braun, E. & Neuringer, L. J. Trigonal Warping of the Energy Surfaces in Tellurium. *Phys Rev B* **2**, 1553–1555 (1970).

39. Niu, C. *et al.* Gate-tunable strong spin-orbit interaction in two-dimensional tellurium probed by weak antilocalization. *Phys Rev B* **101**, (2020).

40. Sudo, K. *et al.* Valley polarization dependence of nonreciprocal transport in a chiral semiconductor. *Phys Rev B* **108**, (2023).

41. Rikken, G. L. J. A. & Avarvari, N. Strong electrical magnetochiral anisotropy in tellurium. *Phys Rev B* **99**, (2019).

42. Grosso, G. & Parravicini, G. P. *Solid State Physics*. (Academic Press, 2013).

43. Betbeder-Matibet, O. & Hulin, M. A. Semi-Empirical Model for the Valence Band Structure of Tellurium. *physica status solidi (b)* **36**, 573–586 (1969).

44. Doi, T., Nakao, K. & Kamimura, H. The Valence Band Structure of Tellurium. I. The k·p Perturbation Method. *J Physical Soc Japan* **28**, 36–43 (1970).

45. Kenji, N., Takao, D. & Hiroshi, K. The Valence Band Structure of Tellurium. III. The Landau Levels. *J Physical Soc Japan* **30**, 1400–1413 (1971).

46. Braun, E., Neuringer, L. J. & Landwehr, G. Valence Band Structure of Tellurium from Shubnikov-de Haas Experiments. *physica status solidi (b)* **53**, 635–650 (1972).

47. E. Ivchenko and G. Pikus. Natural optical activity of semiconductors (te). *Sov. Phys. Solid State* **16**, 1261 (1975).

48. Stolze, H., Lutz, M. & Grosse, P. The Optical Activity of Tellurium. *physica status solidi (b)* **82**, 457–466 (1977).

49. L. Dubinskaya and I. Farbstein. Natural optical activity and features of the structure of the electronic energy spectrum of tellurium. *Soviet Physics - Solid State* **20**, 437 (1978).

50. Furukawa, T., Shimokawa, Y., Kobayashi, K. & Itou, T. Observation of current-induced bulk magnetization in elemental tellurium. *Nat Commun* **8**, 954 (2017).

51. Şahin, C., Rou, J., Ma, J. & Pesin, D. A. Pancharatnam-Berry phase and kinetic magnetoelectric effect in trigonal tellurium. *Phys Rev B* **97**, 205206 (2018).

52. Golub, L. E., Ivchenko, E. L. & Spivak, B. Electrical magnetochiral current in tellurium. *Phys Rev B* **108**, 245202 (2023).

53. Chang, M.-C. & Niu, Q. Berry phase, hyperorbits, and the Hofstadter spectrum: Semiclassical dynamics in magnetic Bloch bands. *Phys Rev B* **53**, 7010–7023 (1996).

54. Raoux, A., Piéchon, F., Fuchs, J.-N. & Montambaux, G. Orbital magnetism in coupled-bands models. *Phys Rev B* **91**, 85120 (2015).

55. Drigo, E. & Resta, R. Chern number and orbital magnetization in ribbons, polymers, and single-layer materials. *Phys Rev B* **101**, 165120 (2020).

56. Hara, D., Bahramy, M. S. & Murakami, S. Current-induced orbital magnetization in systems without inversion symmetry. *Phys Rev B* **102**, 184404 (2020).

57. Kim, K.-W., Jeong, H., Kim, J. & Jin, H. Vertical transverse transport induced by hidden in-plane Berry curvature in two dimensions. *Phys Rev B* **104**, L081114- (2021).

58. Lee, S., Shin, J., Jeong, H. & Jin, H. Quantum geometric tensor from real-space twists of chiral chains. *Phys Rev B* **110**, 195139 (2024).

59. Gao, Y. Semiclassical dynamics and nonlinear charge current. *Front Phys (Beijing)* **14**, 33404 (2019).

60. Liu, X., Souza, I. & Tsirkin, S. S. Electrical magnetochiral anisotropy in trigonal tellurium from first principles. (2023).

61. Okumura, S., Tanaka, R. & Hirobe, D. Chiral orbital texture in nonlinear electrical conduction. *Phys Rev B* **110**, L020407- (2024).

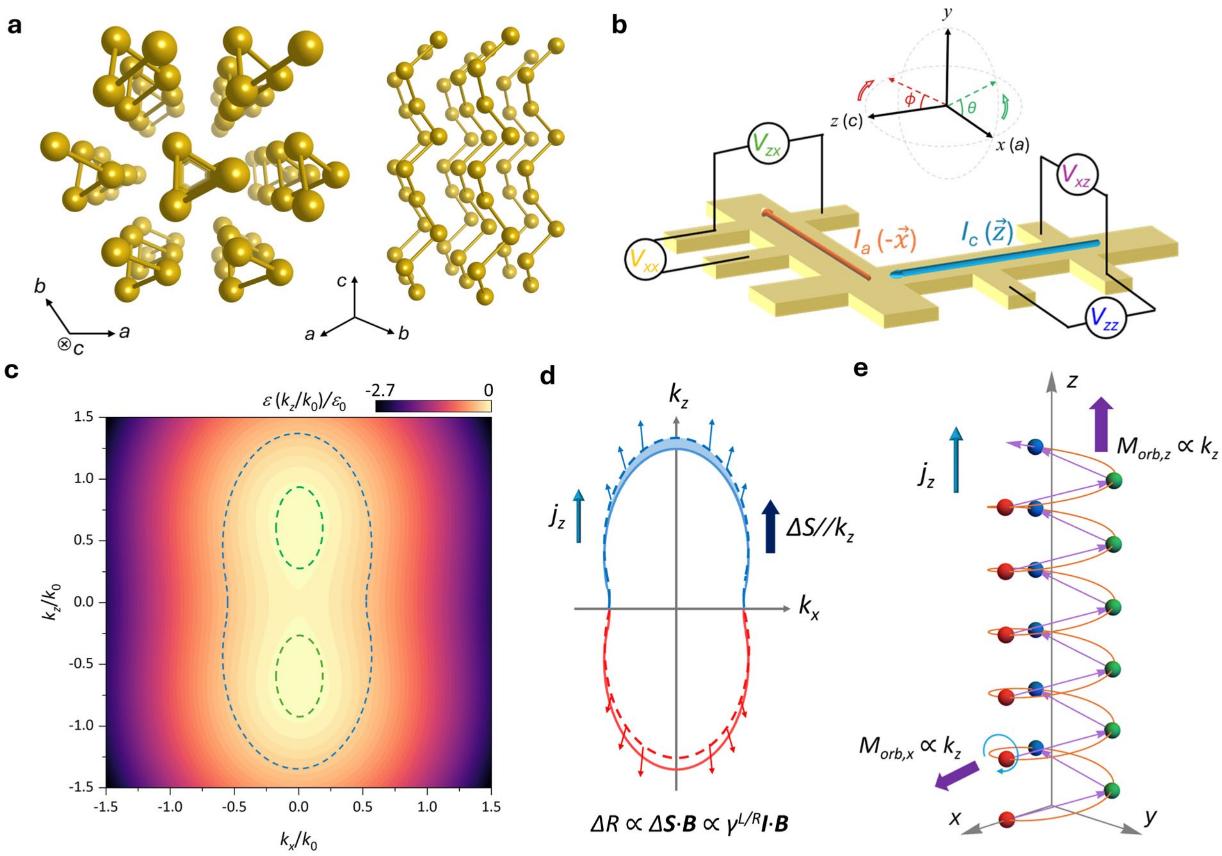
a
b
⊗c
a
c
a
b
b
y
z (c)
x (a)
ϕ
θ
$V_{zx}$
$V_{xx}$
$V_{xz}$
$V_{zz}$
$I_a(-\vec{x})$
$I_c(\vec{z})$
c
$\varepsilon(k_z/k_0)/\varepsilon_0$
-2.7
0
1.5
1.0
0.5
0.0
-0.5
-1.0
-1.5
$k_z/k_0$
-1.5
-1.0
-0.5
0.0
0.5
1.0
1.5
$k_x/k_0$
d
$k_z$
$j_z$
$\Delta S//k_z$
$k_x$
$\Delta R \propto \Delta \boldsymbol{S}\cdot\boldsymbol{B} \propto \gamma^{L/R}\boldsymbol{I}\cdot\boldsymbol{B}$
e
z
$M_{orb,z} \propto k_z$
$j_z$
$M_{orb,x} \propto k_z$
x
y

Fig. 1 | **Chiral crystal trigonal Te. a**, crystal structure of left-handed Te. **b**, schematic of the 'L'-bar device structure, with the two long bars aligned along the crystalline axes labeled as *c* (helical axis) and *a*. The sample can be rotated over 360° in two directions, as illustrated. **c**, calculated energy dispersion of the valence band of Te based on our theoretical model. **d**, illustration of radial spin texture and current-induced spin polarization ($\Delta\boldsymbol{S}$) in Te. The change in resistance ($\Delta R$) switches sign with variations in handedness ($\gamma^L = -\gamma^R$), current direction, or magnetic field orientation. **e**, illustration of current-induced orbital magnetization, where both components along ($\boldsymbol{M}_{orb,z}$) and perpendicular ($\boldsymbol{M}_{orb,x}$) to the helical axis and proportional to $k_z$ are demonstrated.

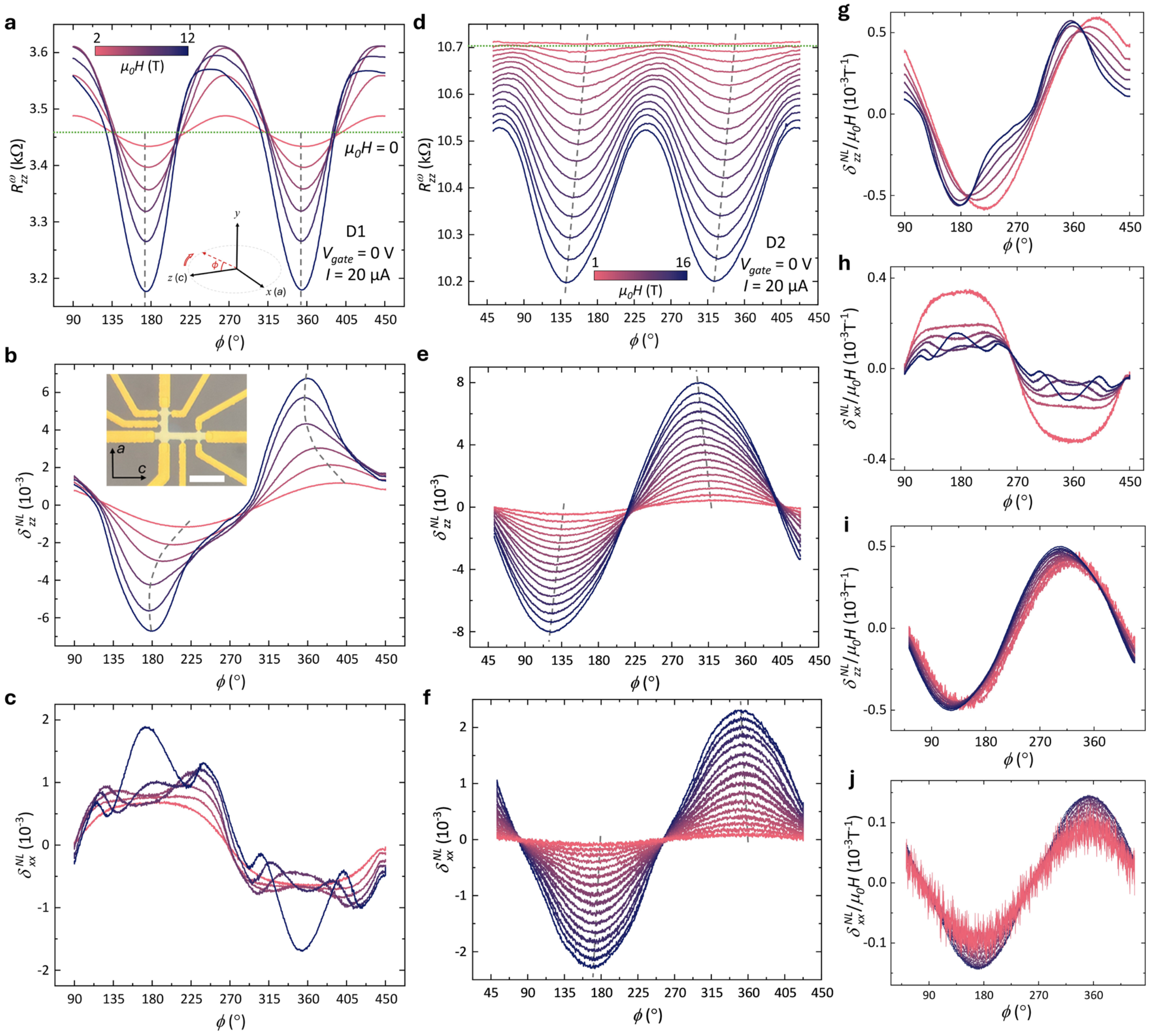

Fig. 2 | **Linear and nonlinear magnetotransport of Te. a-c**, angular dependence of $R^{\omega}_{zz}$ (**a**), $\delta^{NL}_{zz}$ (**b**), and $\delta^{NL}_{xx}$ (**c**) under in-plane rotation of the applied magnetic field ranging from 2 T to 12 T in increments of 2 T, measured in D1 without an applied gate voltage. The current bias is 20 µA. The inset in (**b**) is an optical image of the device (scale bar: 30 µm). **d-f** angular dependence of $R^{\omega}_{zz}$ (**d**), $\delta^{NL}_{zz}$ (**e**), and $\delta^{NL}_{xx}$ (**f**) of D2 under similar measurement conditions while the magnetic fields ranging from 1 T to 16 T in increments of 1 T. $R^{\omega}$ and $\delta^{NL}$ shows contrasting behavior between D1 and D2, where the observations in D2 are beyond the framework of collinear spin polarization. **g-j** magnetic field normalized data of (**b**), (**c**), (**c**) and (**f**).

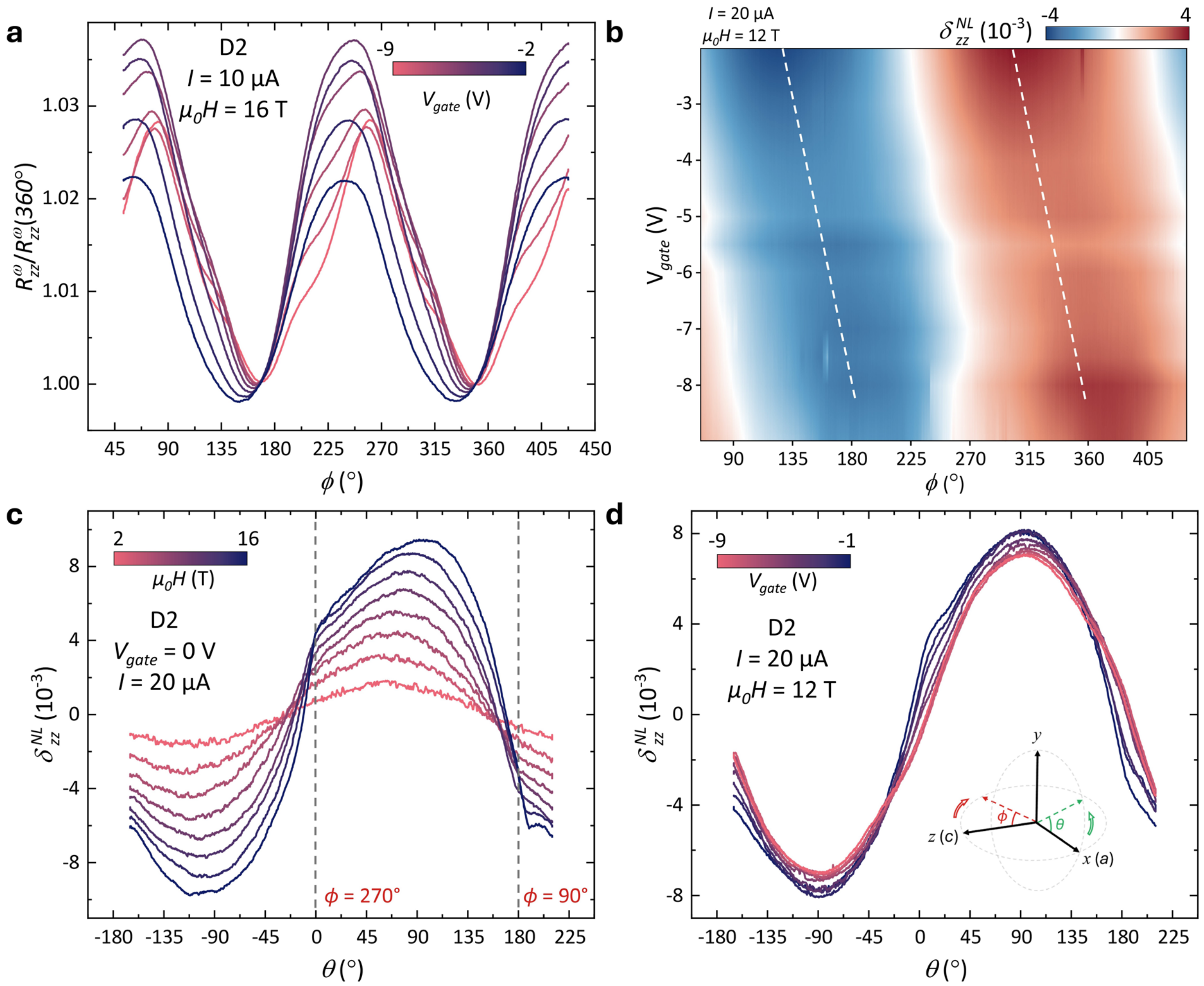

Fig. 3 | **Transition from orbital effect dominant to spin polarization dominant magnetotransport. a**, angular dependence of $R_{zz}^{\omega}$ under different gate voltages. The angular shift of the minima vanishes at sufficiently low $V_{gate}$. **b**, gate voltage mapping of $\delta_{zz}^{NL}$ for $I_c$ = 20 μA and $\mu_0 H$ = 12 T, clearly showing the transition from the proposed orbital magnetization effect dominant region to a spin polarization dominant region, indicated by white dashed lines. **c**, $\theta$-dependence of $\delta_{zz}^{NL}$ under out-of-plane field rotation at $V_{gate}$ = 0 V, the magnetic field is incremented by 2 T. **d**, $\theta$-dependence of $\delta_{zz}^{NL}$ under different gate voltages, demonstrating the crossover between orbital and spin contributions. The hump at $\theta = 0^{\circ}$ and the dip at $\theta = 180^{\circ}$ disappear in the spin polarization-dominant region, where the angular shift also vanishes at that applied magnetic field and current.

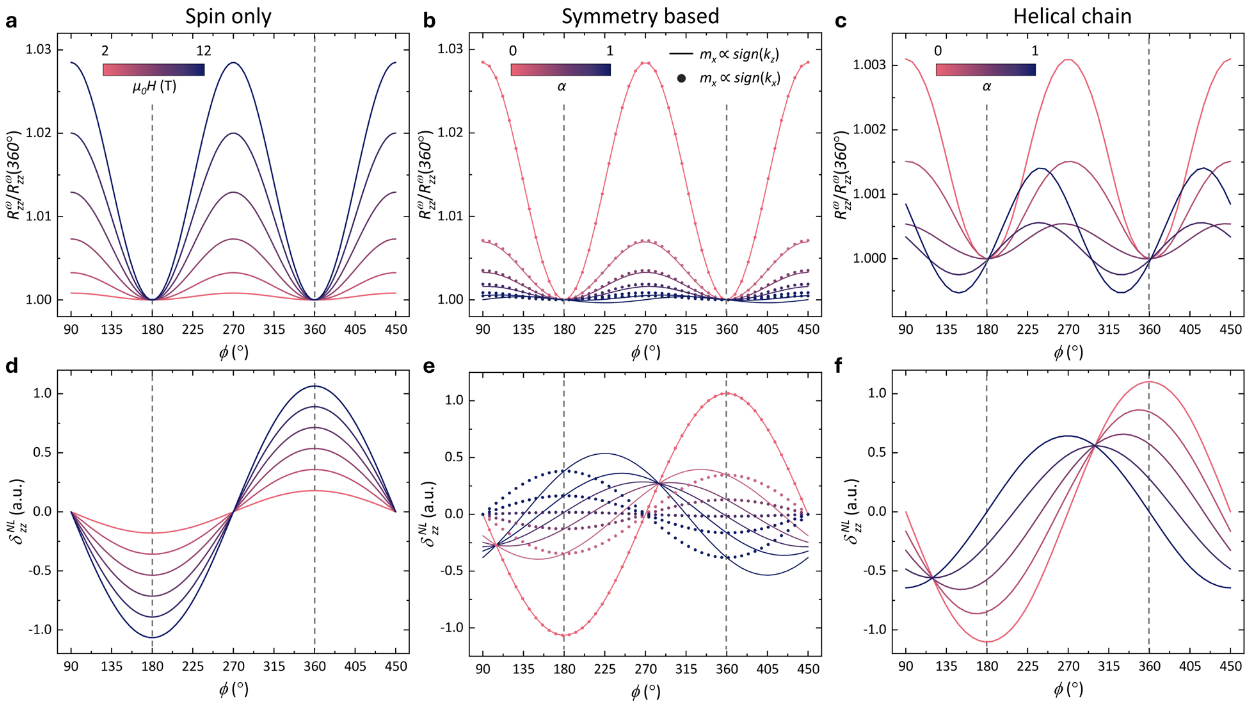

Fig. 4 **| Theoretical plots of linear and non-linear transport:** These figures show linear and non-linear resistivity as a function of the direction of the in-plane magnetic field, calculated using the Boltzmann semiclassical transport formalism (see Supplementary Information for the details of the calculation). **a&d** we consider an energy dispersion that includes only the Zeeman coupling to the spin texture. Here, varying the magnetic field strength does not shift the minima of the oscillations corresponding to the collinear and anti-collinear directions. **b&e**, we introduce an orbital magnetization along the *x*-direction, assumed to be odd in $\boldsymbol{k}_z$ (the figure also includes a component odd in $\boldsymbol{k}_x$, which does not reproduce the observed trend), inspired by the solenoidal model. This leads to a clear shift in the position of the minima. **c&f.** A minimal chiral chain model for helical Te qualitatively captures the same behavior. In these four figures, $\alpha$ is a tuning parameter that controls the relative contribution of spin texture and orbital magnetization to the Zeeman energy: $\alpha = 0$ corresponds to the case with no orbital magnetization (same as the first set), while $\alpha = 1$ corresponds to a scenario with no spin polarization.

# Methods

## Sample and device fabrication

Single crystal Te were grown using a hydrothermal synthesis method. In a typical procedure, 0.09 g of $Na_2TeO_3$ (Sigma-Aldrich) and 0.50 g of PVP (Sigma-Aldrich) were fully dissolved in 33 mL of deionized water (18.2 MΩ·cm). Then, 3.33 mL of aqueous ammonia solution (28%, w/w%) (Sigma-Aldrich) and 1.67 mL of hydrazine hydrate (80%, w/w%) (Sigma-Aldrich) were added. After thorough mixing, the solution was placed into a 50 ml Teflon container, sealed in a stainless-steel autoclave, and heated at 180 °C for 30 hours in a furnace. The autoclave was then allowed to cool naturally to room temperature.

The synthesized Te flakes were transferred onto Si/$SiO_2$ wafer with degenerately doped Si and 90 nm thick $SiO_2$ using the Langmuir-Schaefer technique. The 'L'-bar device pattern was defined by photolithography, with a spin-coated layer of photoresist (AZ5214E) and etched using reactive ion etching (50 mTorr Ar, 50 W RF power, 2 mins). Electrodes were patterned in a second photolithography step, followed by the deposition of 80 nm Au using a thermal evaporator.

## Linear and nonlinear electrical measurements.

'L'-bar devices were wired to a customized sample stage made of G-10 using Pt wires and silver paint. The stage was then installed in a Physical Property Measurement System (PPMS, Quantum Design) for transport measurements at temperatures down to 2 K. The sample probe is equipped with a high-precision and low friction rotator which is driven by a DC servomotor, with the angle calculated from the motor steps and calibrated using a Hall sensor (THS118, Toshiba) for each measurement. The a.c. current was injected using Stanford Research CS580 voltage-controlled current source, synchronized with Stanford Research S860 lock-in amplifiers. The lock-in amplifiers were used to measure the fundamental and the second-harmonic voltages. Electrostatic gating is sourced by the Keithley 2450 source-measure unit.

## Linear and nonlinear magnetotransport via a.c. measurements

Linear and non-linear transport coefficients are extracted using an a.c. current. Specifically, an a.c bias current, $I = I_0 \sin\omega t$ at frequency $f = \omega/2\pi = 17.17$ Hz, is applied to the devices (see Extended Data Fig. 1a). The resulting longitudinal voltage can be expressed as

$$\begin{aligned} V &= IR = R^{(0)}I + R^{(1)}I^2 + \cdots \\ &= R^{(0)}I_0 sin\omega t + R^{(1)}I_0^2 sin^2\omega t \\ &= R^{(0)}I_0 sin\omega t + \frac{1}{2}R^{(1)}I_0^2 + \frac{1}{2}R^{(1)}I_0^2 \sin\left(2\omega t - \frac{\pi}{2}\right) \qquad \text{(E1)} \end{aligned}$$

where $R^{(n)}$ represents the $n^{\text{th}}$-order nonlinear resistance term with respect to current, higher-order terms are neglected. The fundamental ($\omega$) and second harmonic ($2\omega$) voltages components are captured by two synchronized lock-in amplifiers at phase 0° and -90°, respectively. Linear and nonlinear magnetotransport are defined as

$$R^{\omega} = \frac{V^{\omega}}{I_0} = R^{(0)},\ \delta^{NL} = \frac{2R^{2\omega}}{R^{\omega}} = \frac{2V^{2\omega}}{V^{\omega}} = \frac{R^{(1)}I_0}{R^{(0)}} \tag{E2}$$

Since linear resistance $R^{(0)}$ (e.g. intrinsic and trivial MR) is even with respect to the magnetic field, we extract its magnetic field symmetric component ($R^{\omega}$) to exclude the regular Hall effect contribution (due to misalignment of the sample orientation to the plane). In contrast, $\delta^{NL}$ arises from spin polarization and orbital magnetization, both of which couple to the magnetic field via Zeeman coupling and are odd under field reversal. Therefore, we take the magnetic field antisymmetrized $\delta^{NL}$ to isolate other effects.

## Resistivity and carrier density along different crystalline axes

The resistivity of Te along $c$-axis ($\rho_{zz}^{\omega}$, solid line) and $a$-axis ($\rho_{xx}^{\omega}$, dashed line) measured on device D3 at different gate voltages is shown in Extended Data Fig. 1b. When no gate voltage is applied or at $V_{gate}$ = -5 V, the Fermi level lies within the bandgap. At $V_{gate}$ = -10 V, it shifts into the camelback region, and at $V_{gate}$ = -20 V, it enters the deep valence band. The resistivities exhibit similar magnitudes (within a factor of 1.5) and follow similar temperature dependencies, regardless of whether the Fermi level lies within the bandgap or inside the valence band. This observed similarity in resistivity along different crystalline axes aligns with previous results obtained from Hall bar devices[35], but contrasts with recent resistivity tensor analyses based on 'sunflower'-shaped devices, which reported significant anisotropy[36]. This discrepancy underscores the critical role of sample geometry in resistivity measurements, as variations in the electric potential distribution between 'sunflower' and Hall bar (L'-bar) configurations lead to differing results[37] and we leave a closer examination of this effect for future work.

Extended Data Figs. 1c and 1d display Hall measurements performed on device D2 at gate voltages ranging from -10 V to 0 V, along the $c$-axis and $a$-axis, respectively. The insets illustrate the sheet hole density for both axes, which exhibit similar magnitudes (in the order of $10^{12}$ $\text{cm}^{-2}$) and gate dependencies. The comparable fundamental characteristics along the helical axis and $a$-axis justify a direct comparison of $R^{\omega}$ and $\delta^{NL}$ between these two orientations.

## Nonlinear current dependence

Based on the above discussion, $R^{\omega}$ is expected to remain constant with current, while $\delta^{NL}$ should vary linearly. However, observed current dependence measured on D1 (Extended Data Fig. 3) and D2 (Extended Data Fig. 4) otherwise, suggesting the presence of higher-order terms. These contributions can also be captured using the same measurement scheme. If the3rd- and 4th- order terms of $R^{(n)}$ are nonzero, Eq. E1 can be rewritten as:

$$
\begin{aligned}
V = IR &= R^{(0)}I + R^{(1)}I^2 + R^{(2)}I^3 + R^{(3)}I^4 + \cdots \\
&= R^{(0)}I_0 sin\omega t + R^{(1)}I_0^2 sin^2\omega t + R^{(1)}I_0^3 sin^3\omega t + R^{(1)}I_0^4 sin^4\omega t \\
&= R^{(0)}I_0 sin\omega t + \frac{1}{2}R^{(1)}I_0^2 + \frac{1}{2}R^{(1)}I_0^2 \sin\left(2\omega t - \frac{\pi}{2}\right) + \frac{3}{4}R^{(2)}I_0^3 sin\omega t - \frac{1}{4}R^{(2)}I_0^3 sin3\omega t \\
&\quad + \frac{3}{8}R^{(3)}I_0^4 + \frac{1}{2}R^{(3)}I_0^4 \sin\left(2\omega t - \frac{\pi}{2}\right) + \frac{1}{8}R^{(3)}I_0^4 \sin\left(4\omega t - \frac{\pi}{2}\right) \qquad \text{(E3)}
\end{aligned}
$$

It is clear from above that, $R^{(2)}$ contributes to $V^{\omega}$, and $R^{(3)}$ enters $V^{2\omega}$. Consequently, the expressions for linear and nonlinear magnetotransport become

$$R^{\omega} = \frac{V^{\omega}}{I_0} = R^{(0)} + \frac{3}{4}R^{(2)}I_0^2,\ \delta^{NL} = \frac{2R^{2\omega}}{R^{\omega}} = \frac{2V^{2\omega}}{V^{\omega}} = \frac{R^{(1)}I_0}{R^{(0)}} + \frac{R^{(3)}I_0^3}{R^{(0)}} \qquad \text{(E4)}$$

## Tunable SOC probed by WL(WAL) measurement

The spin-orbit interaction in Te exhibits high gate tunability[39], as demonstrated by WL and WAL measurements. As SOC introduces an additional phase shift, which can flip the interference from constructive to destructive, leading to a WL to WAL transition. In a typical Hall bar device, a transition from WL to WAL is observed as the Fermi level shifts from the valence band edge to deeper within the valence band (Extended Data Fig. 5). This transition indicates weak SOC near the band edge and stronger SOC in the deeper valence band.

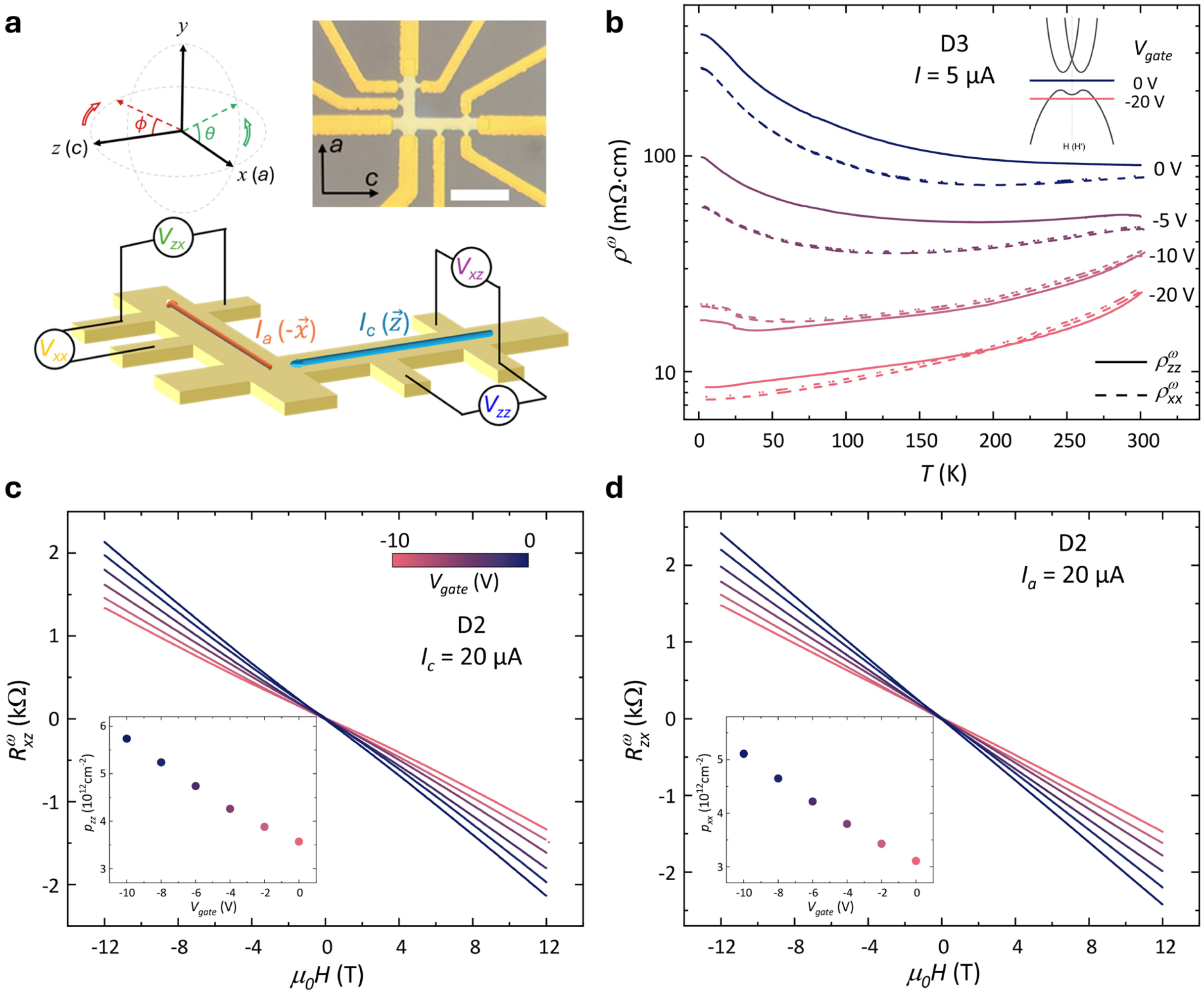

Extended Data Fig. 1 | **a**, illustration of the measurement setup and an optical image of the device. (scale bar: 30 μm). **b**, resistivity along *c*-axis (solid lines) and *a*-axis (dashed lines) at different gate voltages measured on D3, the inset depicts a simplified band structure and indications of Fermi level. **c**, **d**, Hall resistance measured on D2 at different gate voltages along c-axis (**c**) and a-axis (**d**), with insets showing the corresponding sheet hole densities.

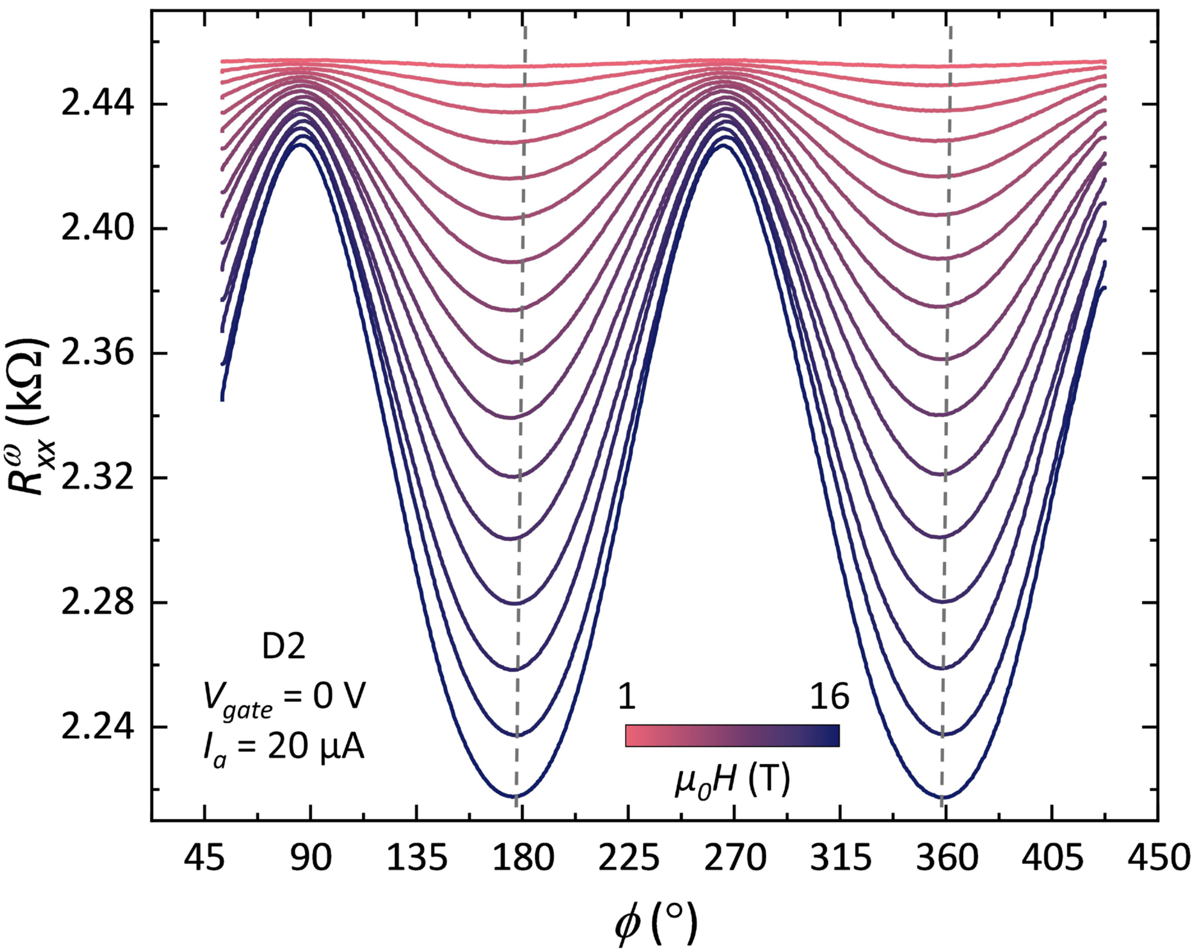

Extended Data Fig. 2 | $R_{xx}^{\omega}$ of D2 measured under in-plane rotation at different magnetic fields, compared to Fig. 2d in the main text. $R_{xx}^{\omega}$ exhibits a smaller angular shift (gray dashed lines).

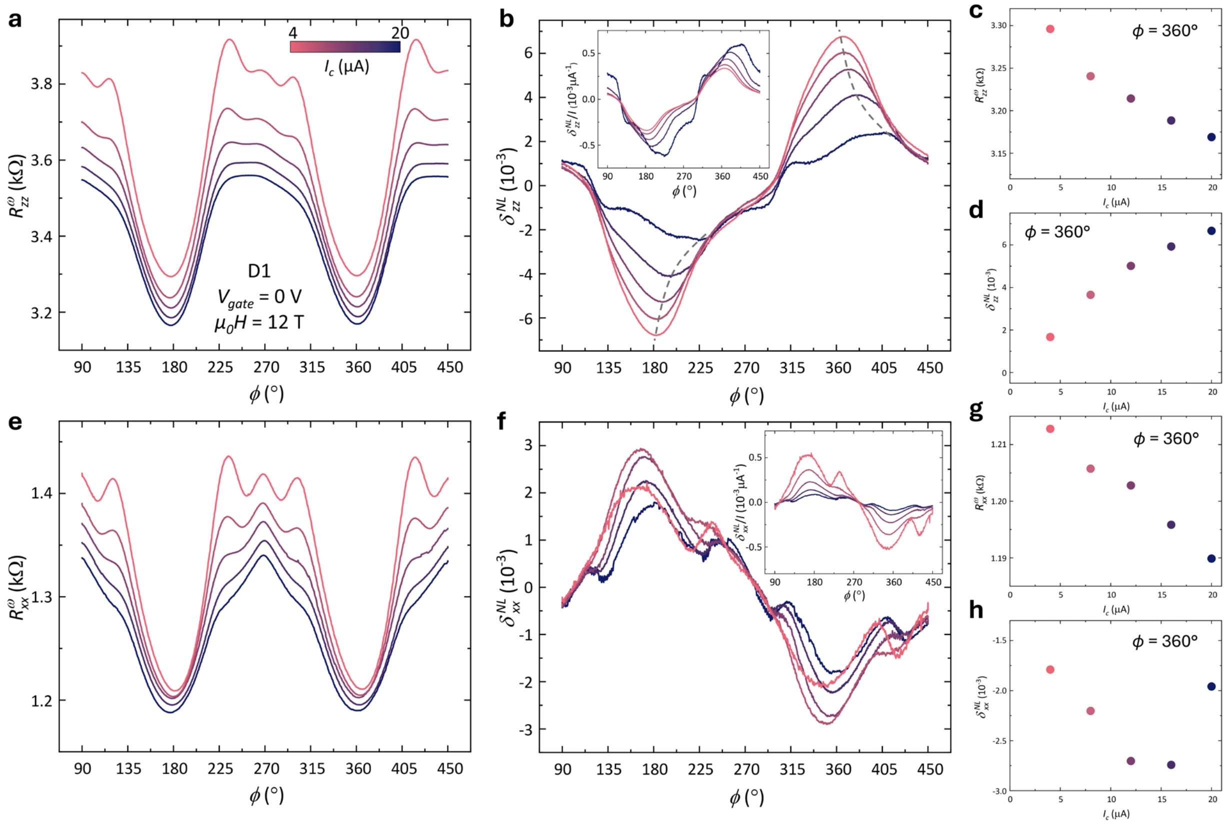

Extended Data Fig. 3 | **a**, **b**, **e**, **f**, $R_{zz}^{\omega}$ (a), $\delta_{zz}^{NL}$ (b), $R_{zz}^{\omega}$ (e), and $\delta_{zz}^{NL}$ (f) measured under in-plane rotation at different current from 4 μA to 20 μA, with an increment of 4 μA. **c, d**, **g**, **h** $R_{zz}^{\omega}$ (c), $\delta_{zz}^{NL}$ (d), $R_{zz}^{\omega}$ (g), and $\delta_{zz}^{NL}$ (h) versus current under 12 T for a fixed angle. The observed nonlinear current dependence can be attributed to high-order terms in Eq. (E4).

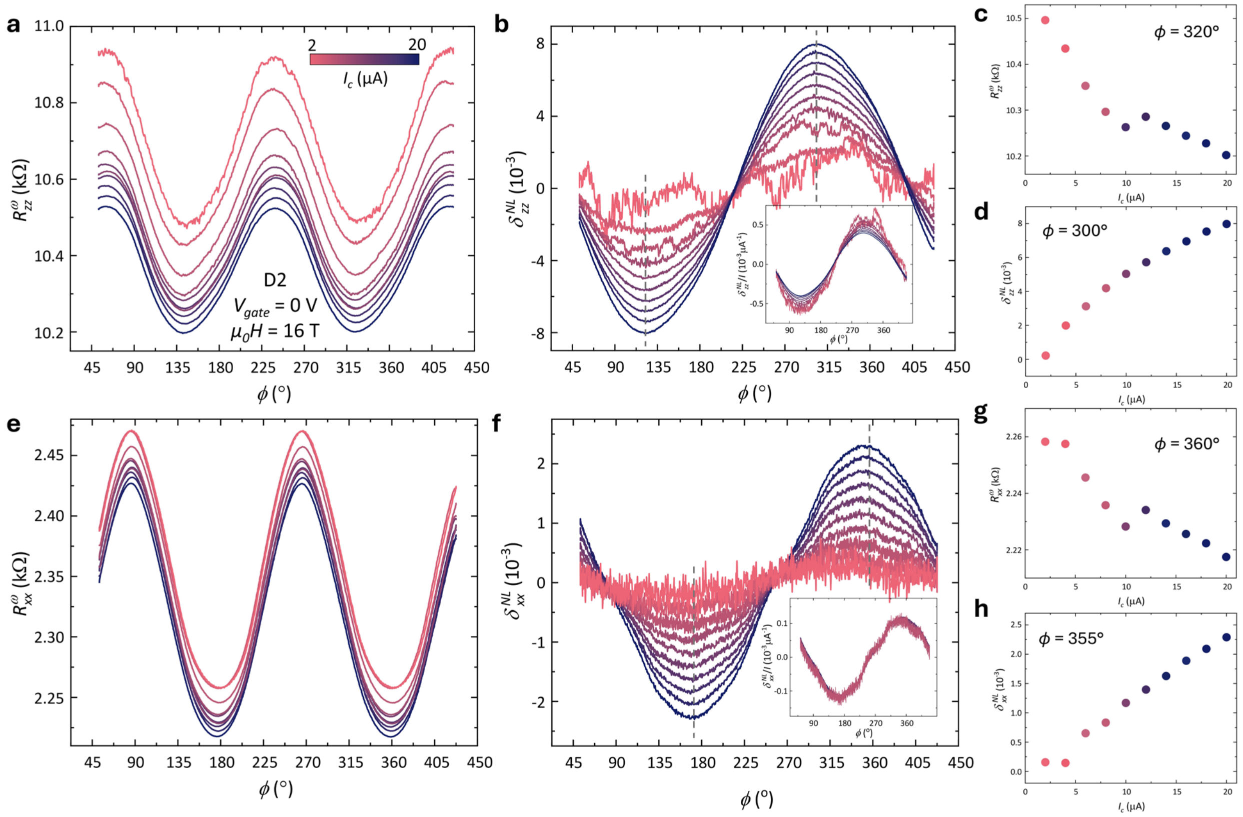

Extended Data Fig. 4 | **a**, **b**, **e**, **f**, $R^{\omega}_{zz}$ (a), $\delta^{NL}_{zz}$ (b), $R^{\omega}_{zz}$ (e), and $\delta^{NL}_{zz}$ (f) measured under in-plane rotation at different current from 2 μA to 20 μA, with an increment of 2 μA. **c, d**, **g**, **h** $R^{\omega}_{zz}$ (c), $\delta^{NL}_{zz}$ (d), $R^{\omega}_{zz}$ (g), and $\delta^{NL}_{zz}$ (h) versus current under 16 T for different fixed angles.

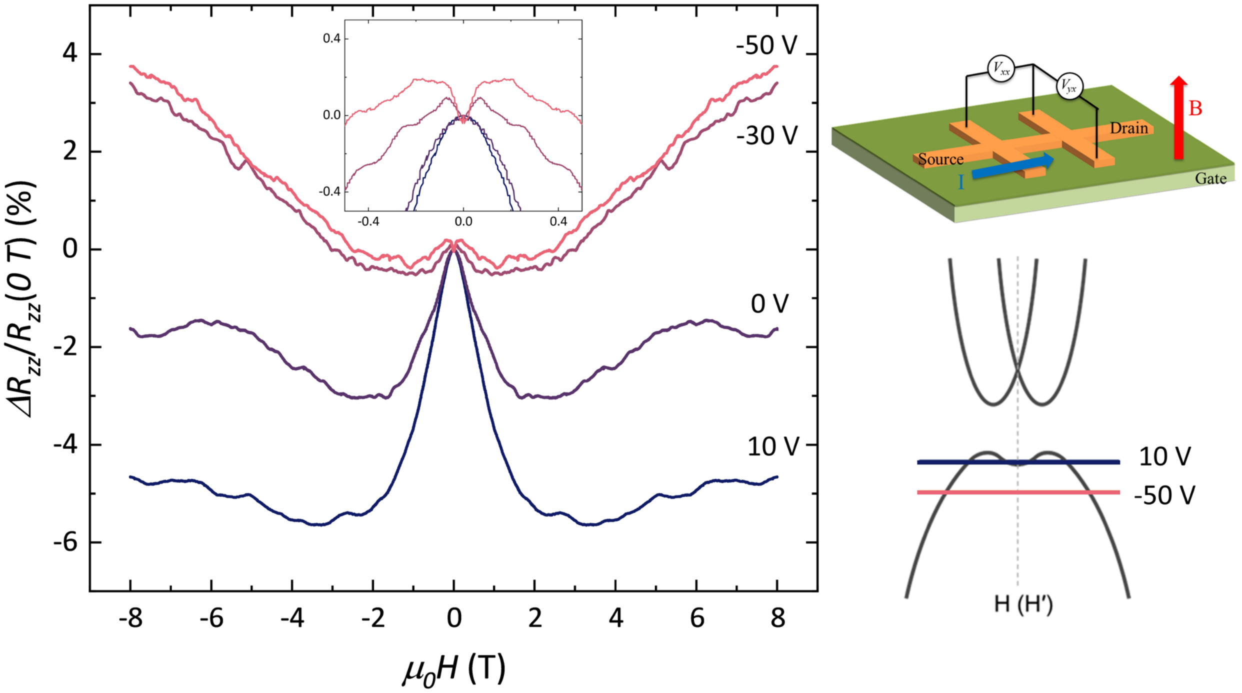

Extended Data Fig. 5 | MR measured on a typical Hall bar Te device (top right), showing a transition from WL to WAL as gate voltage decreases. The inset provides a zoomed-in view, where a clear WAL feature emerges at $V_{gate}$ = -50 V. The bottom right panel illustrates a simplified band structure diagram, depicting the Fermi level positions at different gate voltages.

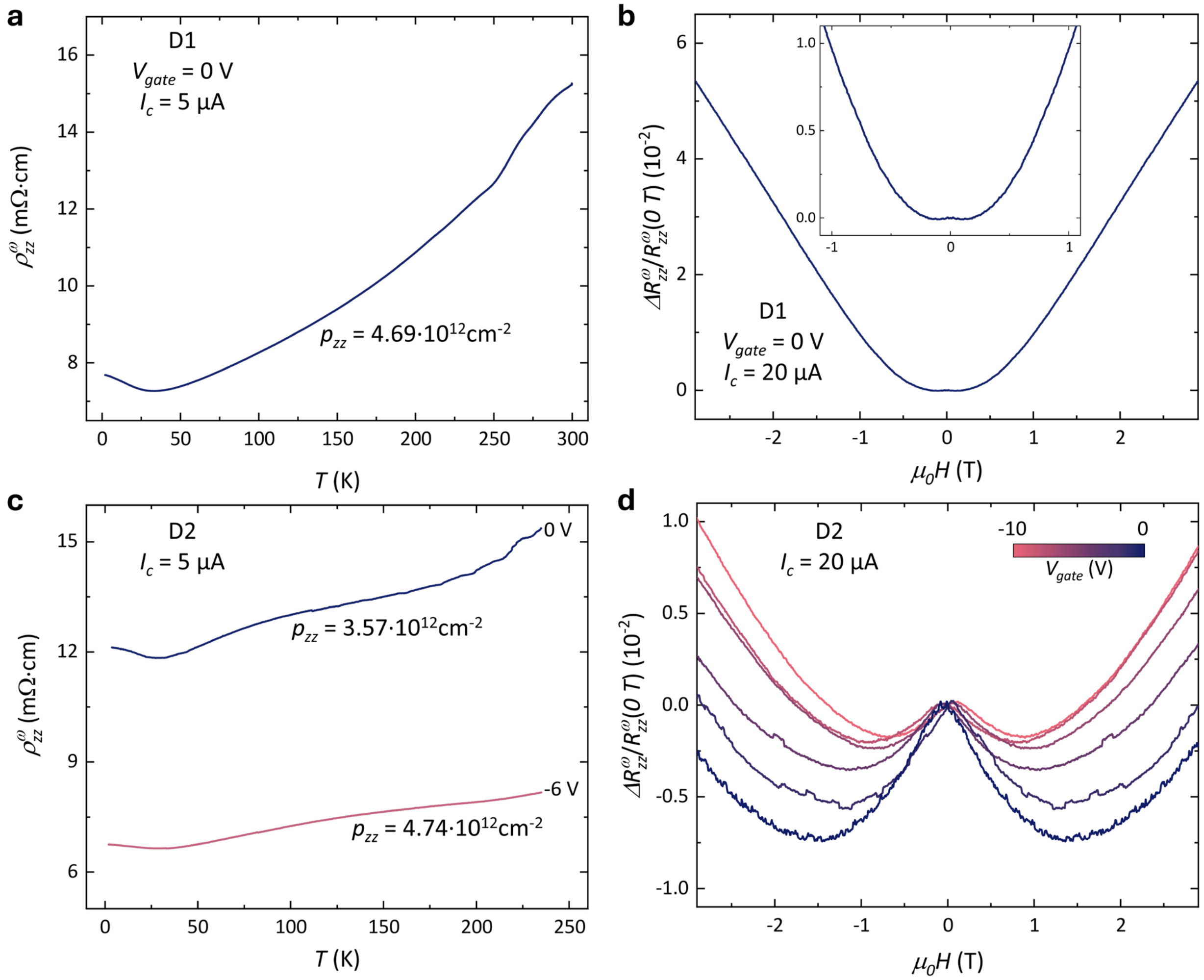

Extended Data Fig. 6 | **a**, **c** Resistivity versus temperature measurements on D1 (**a**) at $V_{gate}$ = 0 V and D2 (**b**) at $V_{gate}$ = 0 V and -6 V, confirming that the Fermi level remains within the valence band across all discussed ranges. Hall measurements indicate a similar carrier density between D1 ($V_{gate}$ = 0 V) and D2 ($V_{gate}$ = -6 V). **b**, **d** Linear longitudinal MR, calculated as $\frac{\Delta R^{\omega}_{zz}}{R^{\omega}_{zz}(0)} = \frac{R^{\omega}_{zz}(\mu_0 H) - R^{\omega}_{zz}(0)}{R^{\omega}_{zz}(0)} \times 100$**,** measured on D1(**b**) and D2 (**d**) under out-of-plane field. The inset in (**b**) provides a zoomed-in view, highlighting the MR lies in the transition region from WL to WAL, indicating strong SOC in D1. In contrast, MR measurements on D2 reveal a strong WL signature, especially at $V_{gate}$ = 0 V, indicating weak SOC. This supports that the behavior observed in Fig. 2d-f originates from orbital effects rather than spin polarization.

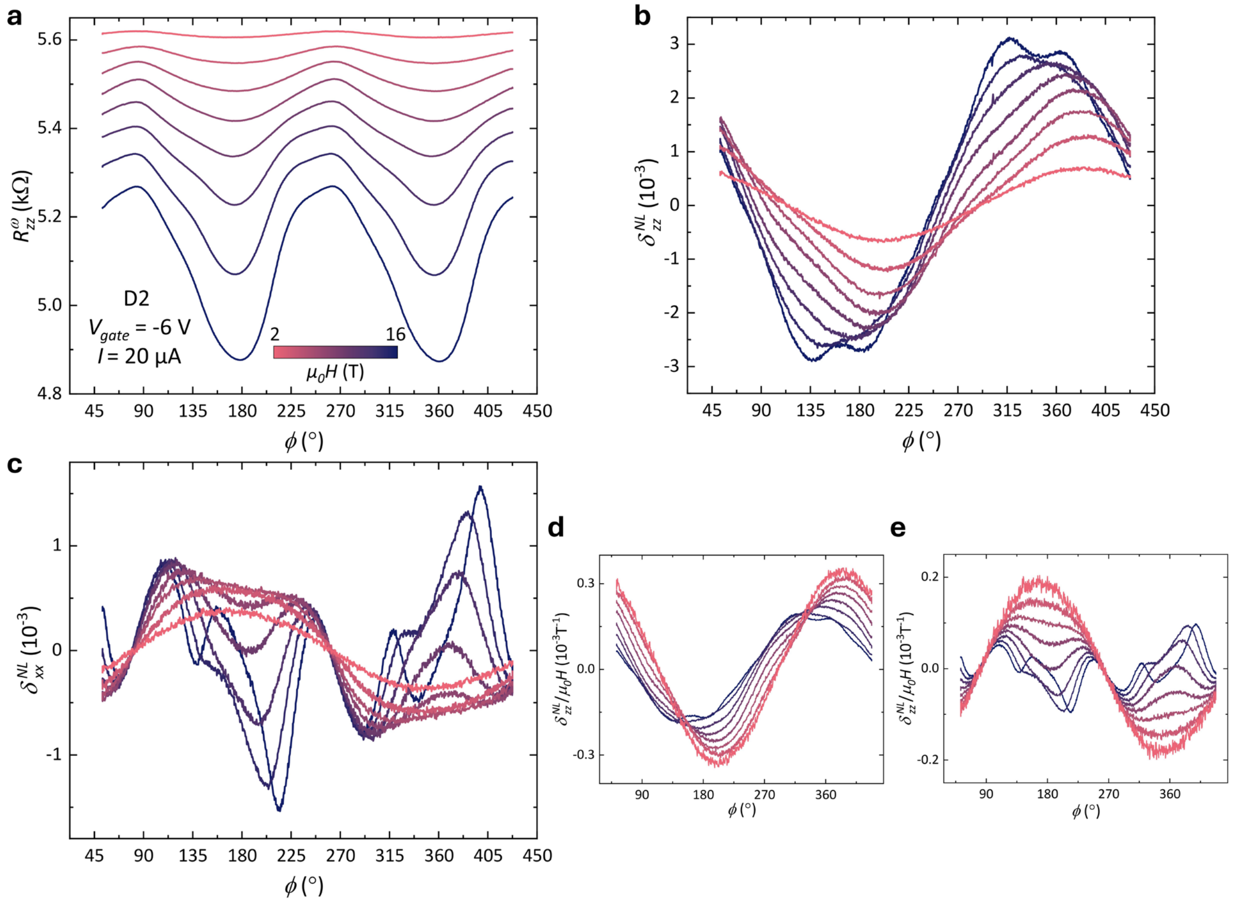

Extended Data Fig. 7 | **a-c** angular dependence of $R_{zz}^{\omega}$ (**a**), $\delta_{zz}^{NL}$ (**b**), and $\delta_{xx}^{NL}$ (**c**) of D2 at $V_{gate}$ = -6 V, measured under magnetic fields ranging from 2 T to 16 T in increments of 2 T. At $V_{gate}$ = -6 V, the carrier density of D2 is comparable to that of D1 at $V_{gate}$ = 0 V, resulting in $R^{\omega}$ and $\delta^{NL}$ exhibiting similar field and angular dependence to those of D1 (Fig. 2a-c), where $\mu_0 H \leq 12$ T. Notably, at higher field (16 T) in (**b**), $\delta_{zz}^{NL}$ exhibit two peaks, supporting the coexistence of spin polarization and orbital magnetization. Meanwhile, $\delta_{xx}^{NL}$ exhibits complex field and angular dependencies, resembling Fig. 2c rather than Fig. 2f, highlighting the contrasting behaviors between different regimes. **d**, **e** normalized data of (**b**) and (**c**), respectively.

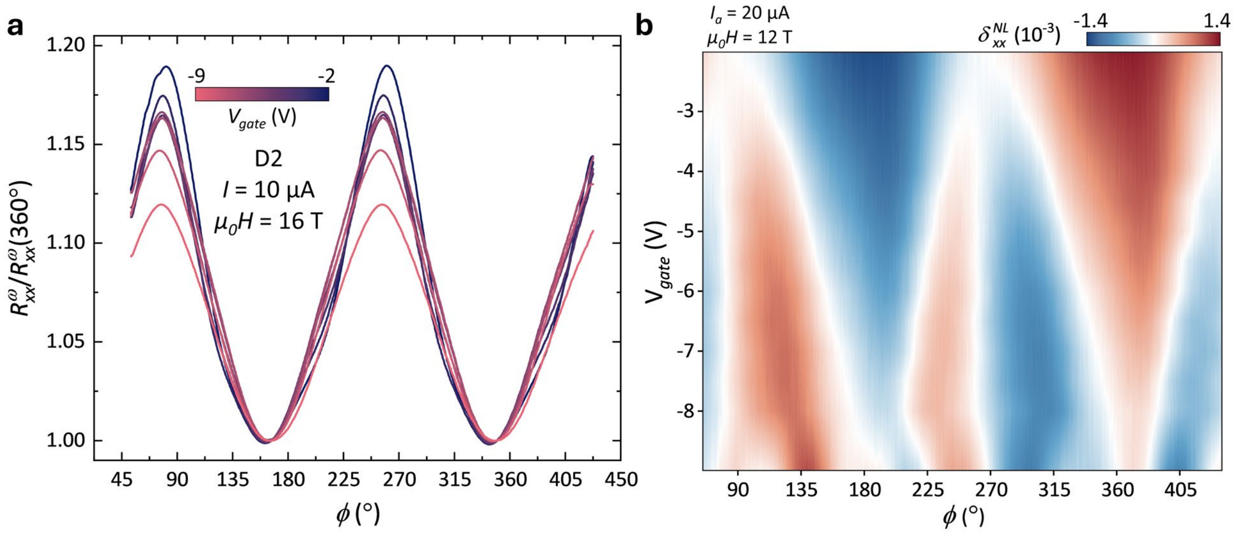

Extended Data Fig. 8 | **a**, angular dependence of $R^{\omega}_{xx}$ under different gate voltages. Unlike $R^{\omega}_{zz}$, the angular shift in $R^{\omega}_{xx}$ approximately remain fixed at ~10° within this gate voltage range. **b**, gate voltage mapping of $\delta^{NL}_{xx}$ for $I_a$ = 20 uA and $\mu_0H$ = 12 T, illustrating the transition of $\delta^{NL}_{xx}$ from weak SOC to strong SOC regions, consistently capturing the previously observed features.

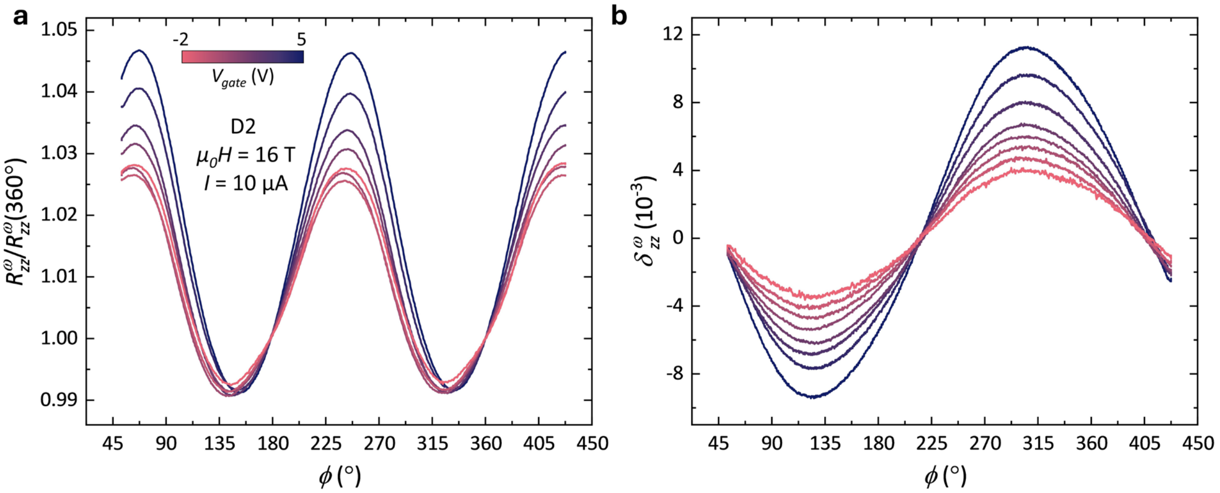

Extended Data Fig. 9 | **a**, **b** angular dependence of $R_{zz}^{\omega}$ (**a**) and $\delta_{zz}^{NL}$ (**b**) under extended gate voltage range (-2 V to 5 V) measured on D2. The angular shift of $R_{zz}^{\omega}$ and $\delta_{zz}^{NL}$ remains fixed, while the amplitude of $\delta_{zz}^{NL}$ continues to increase as SOC weakens, highlighting the significance of orbital effects.

# Supplementary Information for "Interplay of Orbital and Spin Magnetization in Trigonal Tellurium"

Zhenqi Hua [1,2,†], Chang Niu[3,4,†], Sandeep Joy[1,2,†], Pukun Tan[3,4], Gang Shi[1], Haoyang Liu[1], Jiaxing Guo[1], David Graf[2], Peide Ye[3,4], Cyprian Lewandowski[1,2], and Peng Xiong[1]
[1]*Department of Physics, Florida State University, Tallahassee, FL 32306*
[2]*National High Magnetic Field Laboratory, Tallahassee, FL 32310*
[3]*Elmore Family School of Electrical and Computer Engineering, Purdue University, West Lafayette, IN 47907*
[4]*Birck Nanotechnology Center, Purdue University, West Lafayette, IN 47907*

## CONTENTS

S1. Review of linear and non-linear transport 2

S2. Review of theoretical models of Tellurium 3
  S2.A. Phenomenological model 3
  S2.B. Two-band model of Tellurium 4
  S2.C. Six-band model of Tellurium 4

S3. Symmetry analysis of non-linear resistivity: What could give a shift in the minima? 5

S4. One-dimensional Tellurium as a Helical chain: A simplified model 7
  S4.A. Magnetization of current carrying solenoid–an instructive example 7
  S4.B. Modern theory of orbital magnetization in one-dimension 8
  S4.C. Simplified one-dimensional model 9
  S4.D. Minimal Tight-Binding Model – without spin-orbit coupling 9
  S4.E. Minimal Tight-Binding Model – with spin-orbit coupling 10

References 11

## S1. REVIEW OF LINEAR AND NON-LINEAR TRANSPORT

In this section, we outline the main steps in deriving the conductivity tensor in both the linear (electric field-independent) and nonlinear (linear in electric field) regimes. While we aim to keep the discussion as general as possible, we conclude with details specific to tellurium. The derivation of the linear conductivity tensor is standard textbook material, but we include it here for the sake of completeness (for e.g. See Ref [S1]). The standard semiclassical Boltzmann formalism begins with the equations of motion for charge carriers:

$$\dot{\boldsymbol{r}} = \frac{1}{\hbar}\frac{\partial \varepsilon}{\partial \boldsymbol{k}}, \tag{S1}$$

$$\hbar\dot{\boldsymbol{k}} = -e\boldsymbol{E}, \tag{S2}$$

where $\varepsilon$ is the energy dispersion of the carriers. Under the assumptions of spatial homogeneity and the relaxation time approximation ($\tau$), the Boltzmann equation takes the form:

$$\frac{-e\boldsymbol{E}}{\hbar}\cdot\frac{\partial f}{\partial \boldsymbol{k}} = -\frac{f-f^0}{\tau}, \tag{S3}$$

where $f$ is the perturbed distribution function and $f^0$ is the equilibrium distribution function. Knowledge of $f$ allows us to determine the system's response, i.e., its conductivity. We assume that the solution for $f$ can be expanded as a power series in $\boldsymbol{E}$:

$$f = f^0 + f^1 + f^2 + \dots \tag{S4}$$

Substituting the above expansion into the Boltzmann equation, the first- and second-order corrections can be obtained in terms of the equilibrium distribution:

$$f^1 = \frac{eE_\mu\tau}{\hbar}\frac{\partial f^0}{\partial k_\mu}, \tag{S5}$$

$$f^2 = \frac{e^2\tau^2E_\mu E_\nu}{\hbar^2}\frac{\partial^2 f^0}{\partial k_\mu \partial k_\nu}. \tag{S6}$$

These expressions can be used to compute the linear and nonlinear conductivity tensors. The current from a single band is given by integrating the carrier velocity weighted by the distribution function over momentum space:

$$j_\alpha = \frac{1}{(2\pi)^2}\int d\boldsymbol{k}\,(-ev_\alpha)f. \tag{S7}$$

Substituting the series expansion of $f$, we find the linear conductivity tensor:

$$\sigma^0_{\alpha\beta} = \frac{e^2\tau}{(2\pi)^2\hbar}\int d\boldsymbol{k}\left(\frac{\partial\varepsilon}{\partial k_\alpha}\right)\left(\frac{\partial\varepsilon}{\partial k_\beta}\right)\left(-\frac{\partial f^0}{\partial\varepsilon}\right), \tag{S8}$$

and the second-order (nonlinear) conductivity tensor:

$$\sigma^1_{\alpha\beta\gamma} = \frac{e^3\tau^2}{(2\pi)^2\hbar^2}\int d\boldsymbol{k}\,v_\alpha\left(-\frac{\partial^2 f^0}{\partial k_\beta\partial k_\gamma}\right). \tag{S9}$$

Additionally, other contributions to nonlinear conductivity—such as those arising from the Berry curvature dipole, quantum geometry, and skew scattering—are not discussed here [S2]. However, our focus is specifically on the dependence of the (linear) in-plane magnetic field and its orientation on the longitudinal linear and nonlinear response. The other contributions remain unaffected at linear order in the magnetic field [S3, S4]. We should also like to point out that, the results discussed in the main text are carried out for constant chemical potential for all the models. We have verified however that the same trends would be seen if the simulations were plotted for a constant charge density.

In transport experiments, a fixed current is applied and the resulting voltage drop is measured. Consequently, what is directly extracted is the resistivity tensor (or resistance tensor), rather than the conductivity tensor. However, theoretical calculations, such as those based on the Boltzmann formalism, typically yield the conductivity tensor. Below, we present a systematic procedure for inverting the conductivity tensor order by order to obtain the corresponding resistivity tensor. The relation between current density and electric field, expressed in terms of the conductivity and resistivity tensors, is given by:

$$j_\alpha = \sigma^0_{\alpha\beta} E_\beta + \sigma^1_{\alpha\beta\gamma} E_\beta E_\gamma, \tag{S10}$$

and

$$E_\alpha = \rho^0_{\alpha\beta} j_\beta + \rho^1_{\alpha\beta\gamma} j_\beta j_\gamma. \tag{S11}$$

We substitute the components of the electric field $\boldsymbol{E}$ in terms of the current density $\boldsymbol{j}$ and the resistivity tensor into the expression for $j_\alpha$:

$$\begin{aligned} j_\alpha &= \sigma^0_{\alpha\beta} E_\beta + \sigma^1_{\alpha\beta\gamma} E_\beta E_\gamma \\ &= \sigma^0_{\alpha\beta}\left(\rho^0_{\beta\mu} j_\mu + \rho^1_{\beta\mu\nu} j_\mu j_\nu\right) + \sigma^1_{\alpha\beta\gamma}\left(\rho^0_{\beta\mu} j_\mu + \rho^1_{\beta\mu\nu} j_\mu j_\nu\right)\left(\rho^0_{\gamma\lambda} j_\lambda + \rho^1_{\gamma\lambda\eta} j_\lambda j_\eta\right) \\ &= \sigma^0_{\alpha\beta}\rho^0_{\beta\mu} j_\mu + \sigma^0_{\alpha\beta}\rho^1_{\beta\mu\nu} j_\mu j_\nu + \sigma^1_{\alpha\beta\gamma}\rho^0_{\beta\mu}\rho^0_{\gamma\lambda} j_\mu j_\lambda + O\left(j^3\right) \end{aligned} \tag{S12}$$

Solving the term linear in $\boldsymbol{j}$ reproduces the standard result from linear response theory:

$$\sigma^0_{\alpha\beta}\rho^0_{\beta\mu} = \delta_{\alpha\mu}, \tag{S13}$$

i.e., the linear resistivity tensor is the inverse of the linear conductivity tensor. At second order, we identify the resistivity tensor $\rho^1_{\alpha\beta\gamma}$ in terms of the conductivity tensor $\sigma^1_{\alpha\beta\gamma}$ as:

$$\rho^1_{\alpha\beta\gamma} = -\rho^0_{\alpha\mu}\sigma^1_{\mu\nu\lambda}\rho^0_{\nu\beta}\rho^0_{\lambda\gamma}. \tag{S14}$$

It is interesting to note that knowledge of the linear resistivity is required in order to invert the nonlinear conductivity tensor and obtain the nonlinear resistivity tensor.

## S2. REVIEW OF THEORETICAL MODELS OF TELLURIUM

In this section, we summarize various theoretical models of tellurium that have been proposed in the literature. Tellurium has been extensively studied as an elemental semiconductor since the 1970s, owing to its unique chiral crystal structure, band dispersion, spin texture, and particularly its pronounced photogalvanic effects [S5–S11]. The models we discuss in this section include: (a) a phenomenological model capturing the dispersion and associated spin texture, (b) a two-band model—considered either with two copies to reproduce the two valleys in tellurium, or as a single-valley model with a radial spin texture, and (c) a six-band model (again with two copies for the two valleys) that incorporates orbital magnetization. We found that none of these models successfully reproduce the experimentally observed trends in its present form using the Boltzmann transport framework.

### S2.A. Phenomenological model

The bare band dispersion of the valence band in tellurium is given by [S12]

$$\varepsilon_v(\boldsymbol{k}) = -\frac{\hbar^2 k_x^2}{2m} - \frac{\hbar^2 k_z^2}{2m} + \sqrt{\alpha_z^2 k_z^2 + \Delta^2}. \tag{S15}$$

We introduce natural units of momentum and energy defined by the characteristic scales of the bare band structure discussed above:

$$k_0 \equiv \frac{m\alpha_z}{\hbar^2}, \quad \text{and} \quad \varepsilon_0 \equiv \frac{\hbar^2 k_0^2}{2m} = \frac{m\alpha_z^2}{2\hbar^2} = \frac{\alpha_z k_0}{2}. \tag{S16}$$

In terms of these rescaled units, the dispersion becomes

$$\varepsilon \equiv \frac{\varepsilon_v(k_0\boldsymbol{q})}{\varepsilon_0} = -q_x^2 - q_z^2 + \sqrt{4q_z^2 + d^2}, \tag{S17}$$

where $\boldsymbol{q} = \boldsymbol{k}/k_0$ and $d = \Delta/\varepsilon_0$. The numerical values for the energy and momentum scales are:

$$\varepsilon_0 = 3.95 \times 10^{-2}\,\mathrm{eV}, \quad k_0 = 3.29 \times 10^{-2}\,\mathring{\mathrm{A}}^{-1}. \tag{S18}$$

The "radial" spin texture of tellurium introduces a Zeeman coupling to the bare dispersion when an in-plane magnetic field is applied, $\boldsymbol{B} = B_{\|}(\sin\phi, 0, \cos\phi)$ [S12]. The spin texture is given by:

$$\boldsymbol{s} \sim \left(0, 0, \frac{3k_z}{2\sqrt{\alpha_z^2 k_z^2 + \Delta^2}}\right). \tag{S19}$$

The spin texture couples to the magnetic field, contributing the following Zeeman term to the energy dispersion:

$$\begin{aligned} \delta\varepsilon &\sim \frac{\mu_0 B_{\|}}{\varepsilon_0} s_z \cos\phi \\ &\sim \left(\frac{\mu_0 B_{\|}}{\varepsilon_0}\right) \frac{3q_z}{\sqrt{4q_z^2 + d^2}} \cos\phi. \end{aligned} \tag{S20}$$

The corresponding dimensionless parameter and magnetic energy scale are:

$$d \equiv \frac{\Delta}{\varepsilon_0} = 1.51, \quad B_0 \equiv \left(\frac{\mu_0 B_{\|}}{\varepsilon_0}\right) \approx 1.4 \times 10^{-3}, \mathrm{eV/T}. \tag{S21}$$

### S2.B. Two-band model of Tellurium

In the Tellurium literature, a low-energy two-band model is frequently used to describe the valence band [S14, S15]. (Close to the Fermi level, there are six bands in total; we will discuss a six-band model below.) The two-band model, written in the spin basis, is given by:

$$\frac{\hat{H}}{\varepsilon_0} = -\left(q_x^2 + q_z^2\right)\mathbb{I} + 2q_z\sigma_z + d\sigma_x. \tag{S22}$$

Here, $\sigma_x$ and $\sigma_z$ are Pauli matrices. The above given two-band model reproduces the dispersion relation in Eq. S17. Since the Hamiltonian is expressed in the spin basis, one can extract the spin texture of the valence band as follows:

$$s_z = \frac{2q_z}{\sqrt{4q_z^2 + d^2}} \quad \text{and} \quad s_x = \frac{d}{\sqrt{4q_z^2 + d}}. \tag{S23}$$

The two-band model breaks time-reversal symmetry: under time reversal, $s_x$ does not map to $-s_x$, which is not surprising, as the $H$ point around which this low-energy Hamiltonian is expanded is not a time-reversal-invariant momentum point [S14, S16]. In fact, there exists another high-symmetry point $H'$, which is related to $H$ by time reversal and restores time-reversal symmetry. The relation between two valleys implies that $s_x(H) = -s_x(H')$, suggesting that $d$ must change sign between them. A related single-valley version of the model that preserves time-reversal symmetry has been studied in the literature by replacing $d$ with $\mathrm{sign}(q_x), d$, leading to a radial spin texture [S13]. However, even this variant fails to reproduce the experimentally observed shift in the resistivity minima and maxima (see Fig S1).

### S2.C. Six-band model of Tellurium

The most complicated model we considered is a six-band model, which includes four valence bands and two conduction bands [S14]. Here we reproduce the six-band Hamiltonian:

$$h_{\boldsymbol{k}} = \begin{pmatrix} E_0 + \beta_c q_z + \lambda_c & \delta_{1c} q_+^2 + A q_- & 0 & P_1 q_+ & P_3 q_z & P_2 q_- \\ \delta_{1c} q_-^2 + A^* q_+ & E_0 - \beta_c q_z + \lambda_c & P_1 q_- & 0 & P_2 q_+ & -P_3 q_z \\ 0 & P_1 q_+ & \beta_v q_z + \lambda_v & d_2 & 0 & P_4 q_- \\ P_1 q_- & 0 & d_2 & -\beta_v q_z + \lambda_v & P_4 q_+ & 0 \\ P_3 q_z & P_2 q_- & 0 & P_4 q_- & \beta_h q_z - 2d_1 + \lambda_h & \delta_{1h} q_+^2 + B q_- \\ P_2 q_+ & -P_3 q_z & P_4 q_+ & 0 & \delta_{1h} q_-^2 + B^* q_+ & -\beta_h q_z - 2d_1 + \lambda_h \end{pmatrix}. \tag{S24}$$

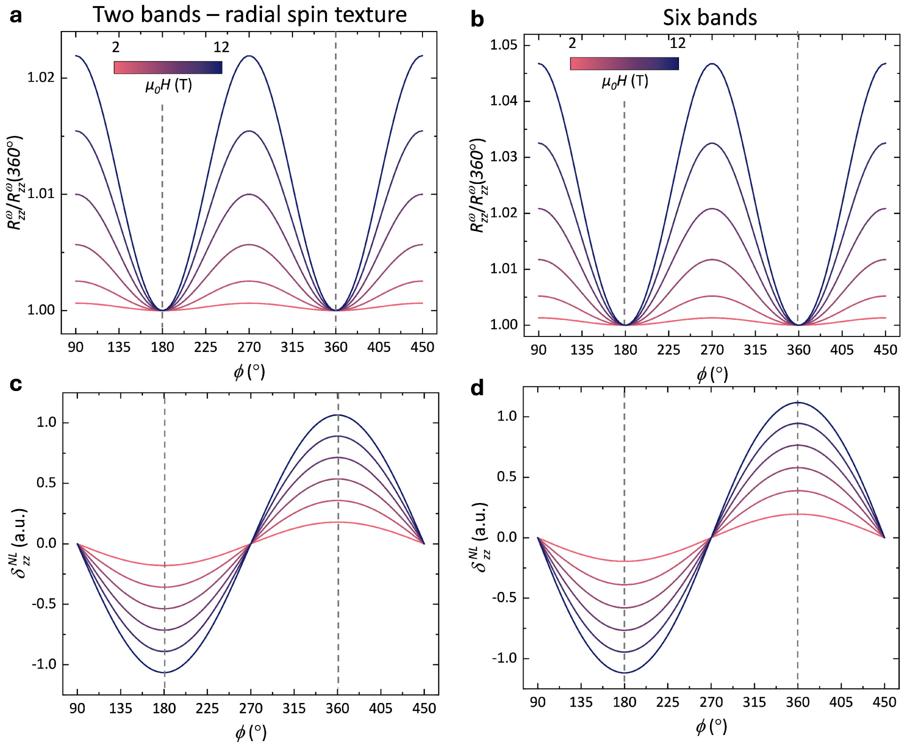

FIG. S1. These figures show the linear and non-linear resistivity as a function of the direction of the in-plane magnetic field, calculated using the Boltzmann semiclassical transport formalism. Panels (a) and (c) correspond to an energy dispersion that includes Zeeman coupling to the radial spin texture in a single-valley model [S13]. As in Fig. 4(a) and (d) of the main text (which considers two valleys with identical $s_z$ and opposite $s_x$), varying the magnetic field strength does not shift the oscillation minima associated with the collinear and anti-collinear directions. Panels (b) and (d) show results from the six-band model in Eq. S24, which includes two valleys and accounts for both spin and orbital magnetization. Even in this case, the positions of the collinear and anti-collinear minima remain unchanged with increasing magnetic field.

| Symbol | Expression |
|---|---|
| $A$ | $\alpha_c + i\delta_{2c}q_z$ |
| $B$ | $\alpha_h + i\delta_{2h}q_z$ |
| $q_\pm$ | $q_x \pm iq_y$ |
| $q_\perp^2$ | $q_x^2 + q_y^2$ |
| $\lambda_i$ | $\frac{\hbar^2}{2m^i_\parallel}q_z^2 + \frac{\hbar^2}{2m^i_\perp}q_\perp^2$ |

TABLE I. List of symbols used in the Hamiltonian in Eq. S24 and their expressions.

The symbols and parameters in Eq. S24 are given in Table I and Table II.

The six-band model reduces to the two-band Hamiltonian (Eq. S22) upon projection onto the top two valence bands and exhibits an analogous spin texture. Unlike the previous models however it has non-zero orbital magnetization [S14, S17], which is plotted in Fig S2 along with their spin-magnetization. Specifically, we find that the model has a non-zero $m_z$ component of orbital magnetization that is odd under momentum $q_z$. The $m_x$ however has not such symmetry and thus does not reproduce the shift from the collinear and anti-collinear directions (see Fig S1) - see also the discussion of the next section.

## S3. SYMMETRY ANALYSIS OF NON-LINEAR RESISTIVITY: WHAT COULD GIVE A SHIFT IN THE MINIMA?

Breaking inversion symmetry is essential for generating a nonzero nonlinear response. Here, we aim to identify the minimal ingredients necessary to account for the experimentally observed trends in the positions of resistivity minima and maxima. In

| Parameter | Value | Parameter | Value |
|---|---|---|---|
| $\beta_v$ | $1.99\,\varepsilon_0 \cdot k_0^{-1}$ | $E_0$ | $10\,\varepsilon_0$ |
| $\beta_c$ | $-0.63\,\varepsilon_0 \cdot k_0^{-1}$ | $\alpha_c$ | $0.055\,\varepsilon_0 \cdot k_0^{-1}$ |
| $\beta_h$ | $0.22\,\varepsilon_0 \cdot k_0^{-1}$ | $\alpha_h$ | $0.039\,\varepsilon_0 \cdot k_0^{-1}$ |
| $P_1$ | $2.79\,\varepsilon_0 \cdot k_0^{-1}$ | $\delta_{1c}$ | $0.010\,\varepsilon_0 \cdot k_0^{-2}$ |
| $P_2$ | $2.95\,\varepsilon_0 \cdot k_0^{-1}$ | $\delta_{2c}$ | $0.062\,\varepsilon_0 \cdot k_0^{-2}$ |
| $P_3$ | $1.66\,\varepsilon_0 \cdot k_0^{-1}$ | $\delta_{1h}$ | $0.003\,\varepsilon_0 \cdot k_0^{-2}$ |
| $P_4$ | $1.61\,\varepsilon_0 \cdot k_0^{-1}$ | $\delta_{2h}$ | $0.024\,\varepsilon_0 \cdot k_0^{-2}$ |
| $\frac{\hbar^2}{2m^v_\parallel}$ | $-0.99\,\varepsilon_0 \cdot k_0^{-2}$ | $\frac{\hbar^2}{2m^v_\perp}$ | $-0.89\,\varepsilon_0 \cdot k_0^{-2}$ |
| $\frac{\hbar^2}{2m^c_\parallel}$ | $1.45\,\varepsilon_0 \cdot k_0^{-2}$ | $\frac{\hbar^2}{2m^c_\perp}$ | $1.57\,\varepsilon_0 \cdot k_0^{-2}$ |
| $\frac{\hbar^2}{2m^h_\parallel}$ | $-0.93\,\varepsilon_0 \cdot k_0^{-2}$ | $\frac{\hbar^2}{2m^h_\perp}$ | $-1.26\,\varepsilon_0 \cdot k_0^{-2}$ |
| $d_1$ | $1.34\,\varepsilon_0$ | $d_2$ | $1.51\,\varepsilon_0$ |

TABLE II. List of parameters used in the Hamiltonian in Eq. S24 and their values. As defined previously, $\varepsilon_0 = 3.95 \times 10^{-2}$ eV, $k_0 = 3.29 \times 10^{-2}$ Å$^{-1}$

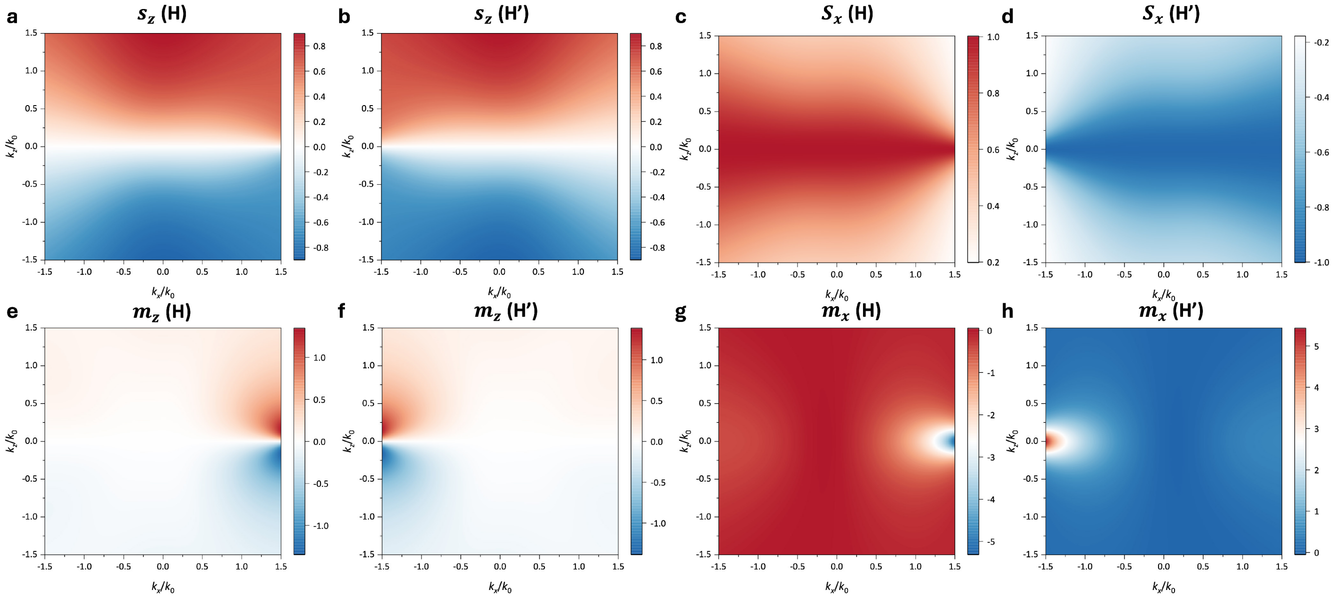

FIG. S2. The orbital $m_{x/z}$ and spin $s_{x/z}$ magnetization calculated from the Hamiltonian in Eq. S24 is plotted. Title subscript in figure title denotes valley $H/H'$, which are related to each other by $d_2 \to -d_2$.

particular, we motivate the need for an orbital magnetization along the $x$-direction that is odd in $q_z$, a feature that naturally emerges in the helical chain model introduced later.

The dispersion of the valence band in the presence of a magnetic field includes a Zeeman coupling term, which gives rise to magnetotransport. Let us examine this more carefully. The magnetic field dependent part of the dispersion takes the form (remember $B_0 \equiv (\mu_0 B_\parallel/\varepsilon_0)$):

$$\delta\varepsilon = -B_0 \cos\phi(s_z + m_z) - B_0 \sin\phi(s_x + m_x)\,, \tag{S25}$$

which can be recast as:

$$\delta\varepsilon = -B_0 \sqrt{(s_z + m_z)^2 + (s_x + m_x)^2}\cos(\phi - \phi_0), \tag{S26}$$

where

$$\phi_0 = \arctan\left[\frac{s_x + m_x}{s_z + m_z}\right]. \tag{S27}$$

To ensure that the linear magnetoresistance $\rho_{zz}$ is 180°-periodic (mandated by the time-reversal symmetry of the equilibrium state since Tellurium is non-magnetic), the vector $\boldsymbol{m}$ must be odd under $\boldsymbol{q}$, thereby preserving time-reversal symmetry. Given the helical chain structure of tellurium, a natural candidate for $\boldsymbol{m}$ is the orbital magnetization of the Bloch states, arising from the solenoidal character of the system. The above Eq. (S27) also shows that unless the system has a non-zero spin or orbital magnetization along the $x$ direction, the maxima/minima of the dispersion are locked to the collinear/anti collinear directions (i.e.$\phi_0 = 0, 180°$). One could also imagine a magnetization term along the $x$-direction that is odd under $q_x$. However, as shown in Fig. 4(b) and (e) of the main text, such a term does not shift the minima or maxima away from the collinear and anti-collinear directions. This is consistent with the result in Fig. S1(a) and (c), where an $s_x$ component that is odd under $q_x$ similarly fails to produce any shift.

## S4. ONE-DIMENSIONAL TELLURIUM AS A HELICAL CHAIN: A SIMPLIFIED MODEL

In this section, we discuss the modern theory of orbital magnetization in the context of tellurium, modeled as a chiral helical chain. We begin with a classical example of a solenoid, demonstrating that it possesses orbital magnetization both along the helical axis and perpendicular to it. We then place this intuition on firmer footing using quantum theory. Motivated by these insights, we construct a minimal model based on one-dimensional tellurium chains, which explain the experimentally observed trends of resistivity. We note in passing that the condensed matter analogue of (quantum) solenoid character in tellurium has been previous recognized in the literature [S12, S18, S19].

### S4.A. Magnetization of current carrying solenoid–an instructive example

Since we have argued that the solenoidal nature of tellurium can give rise to orbital magnetization, we first discuss this effect at a classical level to build intuitive understanding (a formal quantum derivation will be provided later). Below, we sketch the derivation of the magnetization for a helical solenoid described by the following equation:

$$\boldsymbol{r}_s = (-a\sin\lambda, a\cos\lambda, c\lambda) \tag{S28}$$

For a perfect solenoid, the ”pitch” $c$ would be zero. The purpose of this exercise is to demonstrate that classically, when the pitch is non-zero, it is possible to have magnetization perpendicular to the direction of helical axes. To that end, we calculate:

$$d\boldsymbol{r}_s = (-a\cos\lambda, -a\sin\lambda, c)\, d\lambda \tag{S29}$$

The magnetization is given by:

$$\boldsymbol{M} = \frac{1}{2}\int \boldsymbol{r}\times d\boldsymbol{I} \tag{S30}$$

In our case,

$$\begin{aligned} \boldsymbol{r}\times d\boldsymbol{I} &= I_0\boldsymbol{r}_s\times d\boldsymbol{r}_s \\ &= d\lambda\Big(ac\left(\cos\lambda+\lambda\sin\lambda\right), -ac\left(-\sin\lambda+\lambda\cos\lambda\right), a^2\Big) \end{aligned} \tag{S31}$$

Component-wise, we find:

$$\begin{aligned} M_x &= \frac{1}{2}acI_0\int_{-2n\pi}^{2n\pi}(\cos\lambda+\lambda\sin\lambda)\, d\lambda, \\ &= -2n\pi acI_0, \end{aligned} \tag{S32}$$

and

$$\begin{aligned} M_y &= -\frac{1}{2}acI_0\int_{-2n\pi}^{2n\pi}(-\sin\lambda+\lambda\cos\lambda)\, d\lambda, \\ &= 0, \end{aligned} \tag{S33}$$

and

$$\begin{aligned} M_z &= \frac{1}{2}a^2 \int_{-2n\pi}^{2n\pi} d\lambda, \\ &= 2n\pi a^2 I_0. \end{aligned} \tag{S34}$$

Magnetization per loop is given by:

$$\frac{\boldsymbol{M}}{2n} = \left(-\pi ac, 0, \pi a^2\right) I_0. \tag{S35}$$

The presence of magnetization along the $x$-direction clearly indicates that a finite pitch induces an in-plane magnetization component perpendicular to the axis of the helical solenoid.

### S4.B. Modern theory of orbital magnetization in one-dimension

Here for completeness we provide a short summary of the modern theory of orbital magnetization that is used to compute magnetization of the helical chain. The notion that a finitely spread wavepacket can exhibit self-rotation around its center of mass underlies the modern theory of orbital magnetization (see Ref [S20], and references therein). The orbital magnetization behaves analogously to spin magnetization, coupling to external magnetic fields through a Zeeman-like interaction. In two-dimensional materials, out-of-plane orbital magnetization has sparked considerable interest over the past few decades. From a classical perspective discussed in the previous section, it is evident that a charged particle undergoing helical motion acquires an orbital magnetic moment at least along its direction of motion. We will demonstrate how this intuition can be placed on firm theoretical footing. The orbital magnetization for a band labeled by index $n$ at momentum $\boldsymbol{q}$ is given by[S20–S22]

$$m_n^a(\boldsymbol{q}) = \frac{ie}{2\hbar} \sum_{m\neq n} \epsilon^{abc} \frac{\langle u_n(\boldsymbol{q})| v^b |u_m(\boldsymbol{q})\rangle \langle u_m(\boldsymbol{q})| v^c |u_n(\boldsymbol{q})\rangle}{\varepsilon_n(\boldsymbol{q}) - \varepsilon_m(\boldsymbol{q})} \tag{S36}$$

where $v^b$ is the velocity operator in the $b$-direction, $|u_n(\boldsymbol{q})\rangle$ is the Bloch wavefunction of the $n^{\text{th}}$ band at momentum $\boldsymbol{q}$, and $\varepsilon_n(\boldsymbol{q})$ is the energy of the $n^{\text{th}}$ band at momentum $\boldsymbol{q}$. In three-dimensional materials, this is typically given by the operator $\partial H/\partial q_b$. In two-dimensional systems lying in the $x$-$y$ plane, this expression implies that the only nonzero component of orbital magnetization is along the $z$-direction. In strictly one-dimensional systems, the expression predicts vanishing orbital magnetization in all directions.

However, care must be taken when defining the velocity operator if any spatial direction is finite—such as in a thin slab of a two-dimensional system or a one-dimensional system with internal structure within the unit cell. The ambiguity can be addressed by defining the velocity operator via the Heisenberg equation of motion:

$$v^a = \frac{-i}{\hbar}\left[x^a, H\right]. \tag{S37}$$

Plugging this into the matrix element of the velocity operator yields

$$\begin{aligned} \langle u_n(\boldsymbol{q})| v^a |u_m(\boldsymbol{q})\rangle &= \langle u_n(\boldsymbol{q})| \frac{-i}{\hbar}\left[x^a, H\right] |u_m(\boldsymbol{q})\rangle \\ &= \frac{i}{\hbar}\left(\varepsilon_n(\boldsymbol{q}) - \varepsilon_m(\boldsymbol{q})\right) \langle u_n(\boldsymbol{q})| x^a |u_m(\boldsymbol{q})\rangle \end{aligned} \tag{S38}$$

The above expression makes it clear that the position operator matrix element in the Bloch basis is ill-defined when the corresponding spatial direction is periodic or infinite. However, in systems that are finite along some directions, this formulation becomes meaningful and can be used to compute the orbital magnetization properly [S22–S26].

To evaluate the orbital magnetization in a one-dimensional chain numerically later, the Bloch wavefunction can be decomposed in the Fourier basis as follows:

$$\begin{aligned} |u_n(\boldsymbol{q})\rangle &= \sum_{\alpha,\sigma} a_{n,\sigma}^{\alpha} |\boldsymbol{q}^{\alpha}, \sigma\rangle \\ &= \frac{1}{\sqrt{N}} \sum_{\alpha,\sigma,j} a_{n,\sigma}^{\alpha} \exp\left[-i\boldsymbol{q}\cdot\boldsymbol{r}_j^{\alpha}\right] |j^{\alpha}, \sigma\rangle, \end{aligned} \tag{S39}$$

where $\sigma$ is the spin index, $\alpha$ labels the atomic position within the unit cell, $j$ labels the unit cell in real space, and $n$ denotes the band index. The coefficient $a^{\alpha}_{n,\sigma}$ are the components of the eigenvectors from diagonalizing the Hamiltonian in the momentum space. The matrix element of the position operator between two Bloch states is then given by:

$$\begin{aligned} \langle u_n(\boldsymbol{q})| x^a |u_m(\boldsymbol{q})\rangle &= \frac{1}{N} \sum_{\alpha,\beta,j,l,\sigma,\sigma'} a^{\alpha}_{n,\sigma} a^{\beta\star}_{m,\sigma'} \exp\left[-i\boldsymbol{q}.\boldsymbol{r}^{\alpha}_{j}\right] \exp\left[i\boldsymbol{q}.\boldsymbol{r}^{\beta}_{l}\right] \left\langle l^{\beta}, \sigma'\right| x^a \left| j^{\alpha}, \sigma\right\rangle \\ &= \frac{1}{N} \sum_{\alpha,\beta,j,l,\sigma,\sigma'} a^{\alpha}_{n,\sigma} a^{\beta\star}_{m,\sigma'} \exp\left[-i\boldsymbol{q}.\boldsymbol{r}^{\alpha}_{j}\right] \exp\left[i\boldsymbol{q}.\boldsymbol{r}^{\beta}_{l}\right] \boldsymbol{r}^a \delta_{jl}\delta_{\alpha\beta}\delta_{\sigma,\sigma'} \\ &= \sum_{\alpha} a^{\alpha}_{n,\sigma} a^{\alpha\star}_{m,\sigma} \boldsymbol{r}^a \end{aligned} \tag{S40}$$

Here, $\boldsymbol{r}^a$ denotes the $a$-th component of the position of atom $\alpha$ within the unit cell.

### S4.C. Simplified one-dimensional model

Given that the symmetry analysis in the previous section suggests the presence of an orbital magnetization along the $x$-direction that is odd in momentum along the (helical) $z$-direction—potentially responsible for the observed trends in both linear and non-linear transport—we now introduce a minimal model of a one-dimensional tellurium chain (Tellurium is known to consist of stacked one-dimensional helical chains.).

We consider a minimal model of a helical chain with three atoms per unit cell, each hosting a single $s$ orbital. While a more realistic model would include four valence orbitals per site (one $s$ and three $p$ orbitals) and account for the orientation of the $p$ orbitals in determining tunneling elements, our simplified model suffices to capture the essential features.

$$\begin{aligned} \boldsymbol{r_1} &= \begin{pmatrix} a & 0 & 0 \end{pmatrix} \\ \boldsymbol{r_2} &= \begin{pmatrix} -\frac{a}{2} & \frac{\sqrt{3}a}{2} & \frac{c}{3} \end{pmatrix} \\ \boldsymbol{r_3} &= \begin{pmatrix} -\frac{a}{2} & -\frac{\sqrt{3}a}{2} & \frac{2c}{3} \end{pmatrix} \end{aligned} \tag{S41}$$

The basis lattice vector is defined as:

$$\boldsymbol{r}^{\alpha}_{j} = \boldsymbol{R}_j + \boldsymbol{r}_{\alpha}, \tag{S42}$$

where

$$\boldsymbol{R}_j = j\boldsymbol{R} = j\begin{pmatrix} 0 & 0 & c \end{pmatrix} \tag{S43}$$

The hopping paths between atoms are given by $\boldsymbol{r}_{ij} = \boldsymbol{r}_i - \boldsymbol{r}_j$.

### S4.D. Minimal Tight-Binding Model – without spin-orbit coupling

The simplest version of the Hamiltonian is a tight-binding model with uniform tunneling between sites:

$$\hat{H} = -t\sum_{j=1}^{N}\left(c^{\dagger}_{j,1}c_{j,2} + c^{\dagger}_{j,2}c_{j,3} + c^{\dagger}_{j,3}c_{j+1,1} + h.c.\right), \tag{S44}$$

where $c_{j,\alpha}$ and $c^{\dagger}_{j,\alpha}$ are annihilation and creation operators at site $\alpha$ in unit cell $j$. Their momentum-space counterparts are defined as:

$$\begin{aligned} c_{j,\alpha} &= \frac{1}{\sqrt{N}}\sum_{\boldsymbol{q}} \exp\left[-i\boldsymbol{q}\cdot\boldsymbol{r}^{\alpha}_{j}\right] c_{\boldsymbol{q},\alpha} \\ c^{\dagger}_{j,\alpha} &= \frac{1}{\sqrt{N}}\sum_{\boldsymbol{q}} \exp\left[i\boldsymbol{q}\cdot\boldsymbol{r}^{\alpha}_{j}\right] c^{\dagger}_{\boldsymbol{q},\alpha} \end{aligned} \tag{S45}$$

Transforming to momentum space, the Hamiltonian becomes:

$$\hat{H} = -t \sum_{\boldsymbol{q}} \begin{pmatrix} c^\dagger_{\boldsymbol{q},1} & c^\dagger_{\boldsymbol{q},2} & c^\dagger_{\boldsymbol{q},3} \end{pmatrix} \begin{pmatrix} 0 & \exp\left[i\boldsymbol{q}\cdot\boldsymbol{r}_{21}\right] & \exp\left[-i\boldsymbol{q}\cdot\boldsymbol{r}_{13}\right] \\ \exp\left[-i\boldsymbol{q}\cdot\boldsymbol{r}_{21}\right] & 0 & \exp\left[i\boldsymbol{q}\cdot\boldsymbol{r}_{32}\right] \\ \exp\left[i\boldsymbol{q}\cdot\boldsymbol{r}_{13}\right] & \exp\left[-i\boldsymbol{q}\cdot\boldsymbol{r}_{32}\right] & 0 \end{pmatrix} \begin{pmatrix} c_{\boldsymbol{q},1} \\ c_{\boldsymbol{q},2} \\ c_{\boldsymbol{q},3} \end{pmatrix} \tag{S46}$$

For our 1D helical chain, we consider only momentum along $z$, i.e.,

$$\boldsymbol{q} = \begin{pmatrix} 0 & 0 & q_z \end{pmatrix}. \tag{S47}$$

Obtaining a simplified Hamiltonian:

$$\hat{H}_{q_z} = -t \begin{pmatrix} 0 & \exp\left[\frac{iq_zc}{3}\right] & \exp\left[-\frac{iq_zc}{3}\right] \\ \exp\left[-\frac{iq_zc}{3}\right] & 0 & \exp\left[\frac{iq_zc}{3}\right] \\ \exp\left[\frac{iq_zc}{3}\right] & \exp\left[-\frac{iq_zc}{3}\right] & 0 \end{pmatrix} \tag{S48}$$

The eigenvalues of this Hamiltonian can be obtained analytically:

$$\varepsilon_\ell\left(q_z\right) = -2t\cos\left(\frac{cq_z}{3} + \frac{2\pi\ell}{3}\right), \tag{S49}$$

where $\ell = 0, \pm 1$ correspond to the three $C_3$ eigenvalues (pseudo-angular momentum). The associated eigenvectors are:

$$|\ell\rangle = \frac{1}{\sqrt{3}} \begin{pmatrix} 1 \\ \exp\left(\ell\frac{i2\pi}{3}\right) \\ \exp\left(-\ell\frac{i2\pi}{3}\right) \end{pmatrix} \tag{S50}$$

While preparing this manuscript, we became aware of an independent study that analyzes the same Hamiltonian, but which focus is on transport along the z-direction [S27]. Unfortunately the model of Eq. (S48) is too minimal to account for the experimental observations, since it only has a orbital magnetization along $z$ direction, $\propto a^2 \sin\left(q_zc/3\right)$. By adding an asymmetry between sites (by onsite energy or inequivalent tunneling terms) one could obtain the orbital magnetization along $x$ and $y$-direction that is odd in $q_z$ - a procedure we follow in the next subsection.

### S4.E. Minimal Tight-Binding Model – with spin-orbit coupling

A spin texture locked to the momentum along the helical axis is a distinctive feature of tellurium. Such a texture can be realized by incorporating spin-orbit coupling into the model. To achieve this, we need the initially spin-degenerate band to split such that spin-up states have energy proportional to $q_z$ and spin-down states to $-q_z$, which can be implemented by introducing a term proportional to $\pm\sin q_z$ for the two spin flavors. Concretely, we add the following term:

$$\hat{H}_{\mathrm{SOC}} = t_I \sum_{j=1}^{N} \sum_{\sigma} \mathrm{sign}(\sigma) \left( ic^\dagger_{j,1,\sigma} c_{j,2,\sigma} + ic^\dagger_{j,2,\sigma} c_{j,3,\sigma} + ic^\dagger_{j,3,\sigma} c_{j+1,1,\sigma} + \mathrm{h.c.} \right), \tag{S51}$$

where sign($\sigma$) distinguishes the spin flavors. To reproduce the approximately constant spin polarization along the $s_x$ direction, we also include an on-site spin-flip term:

$$\hat{H}_{\mathrm{SOC,\ onsite}} = \Delta \sum_{j,\alpha,\sigma\neq\sigma'} c^\dagger_{j,\alpha,\sigma} c_{j,\alpha,\sigma'}. \tag{S52}$$

Finally, by allowing for site-dependent on-site energies $v_\alpha$, we arrive at the general form of the one-dimensional helical chain model. The following model is designed to faithfully capture both the spin and orbital magnetization along $q_z$ near the $H/H'$ points of three-dimensional tellurium:

$$\hat{H}\left(q_z\right) = \begin{bmatrix} v_1 & \Delta & -t_{12}\exp\left[i\Phi\right] & 0 & -t^\star_{31}\exp\left[-i\Phi\right] & 0 \\ \Delta & v_1 & 0 & -t^\star_{12}\exp\left[i\Phi\right] & 0 & -t_{31}\exp\left[-i\Phi\right] \\ -t^\star_{12}\exp\left[-i\Phi\right] & 0 & v_2 & \Delta & -t_{23}\exp\left[i\Phi\right] & 0 \\ 0 & -t_{12}\exp\left[-i\Phi\right] & \Delta & v_2 & 0 & -t^\star_{23}\exp\left[i\Phi\right] \\ -t_{31}\exp\left[i\Phi\right] & 0 & -t^\star_{23}\exp\left[-i\Phi\right] & 0 & v_3 & \Delta \\ 0 & -t^\star_{31}\exp\left[i\Phi\right] & 0 & -t_{23}\exp\left[-i\Phi\right] & \Delta & v_3 \end{bmatrix}. \tag{S53}$$

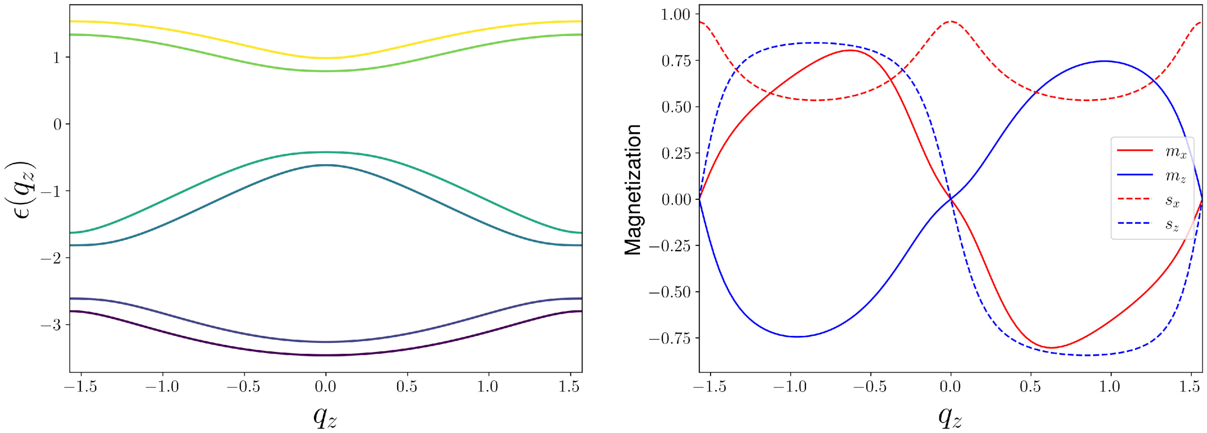

FIG. S3. (a) Band structure calculated from Eq. S53 using the parameters: $t_{12} = 1 + 0.1i$, $t_{23} = 1.1 + 0.1i$, $t_{31} = 1.2 + 0.1i$, $\Delta = 0.1$, $\nu_1 = -2$, $\nu_2 = -1$, $\nu_3 = 0$, and $c = 2$. For the fourth highest energy band, we show the spin and orbital components $s_{x/z}$ and $m_{x/z}$.

For brevity we have defined $\Phi = q_z c/3$.

The current model has two major limitations. First, it is a simplified one-dimensional representation of a three-dimensional material, constructed using symmetry arguments and physical intuition. While it captures the magnetization trends reasonably well and qualitatively explains the experimental observations, a more rigorous ab-initio derivation is necessary for firm justification, and quantitative comparison between theory and experiment. We leave this for future work.

[S1] G. Grosso and G. Parravicini, *Solid State Physics* (Academic Press, 2013).
[S2] D. V. Chichinadze, N. J. Zhang, J.-X. Lin, E. Morissette, X. Wang, K. Watanabe, T. Taniguchi, O. Vafek, and J. I. A. Li, Observation of giant nonlinear hall conductivity in bernal bilayer graphene (2025), arXiv:2411.11156.
[S3] Y. Gao, Semiclassical dynamics and nonlinear charge current, Frontiers of Physics **14**, 33404 (2019).
[S4] X. Liu, I. Souza, and S. S. Tsirkin, Electrical magnetochiral anisotropy in trigonal tellurium from first principles (2024), arXiv:2303.10164.
[S5] O. Betbeder-Matibet and M. Hulin, A. semi-empirical model for the valence band structure of tellurium, Phys. Stat. Sol. **36**, 573 (1969).
[S6] T. Doi, K. Nakao, and H. Kamimura, The valence band structure of tellurium. i. the k·p perturbation method, J. Phys. Soc. Japan **28**, 36 (1970).
[S7] K. Nakao, T. Doi, and H. Kamimura, The valence band structure of tellurium. iii. the landau levels, J. Phys. Soc. Japan **30**, 1400 (1971).
[S8] E. Braun, L. J. Neuringer, and G. Landwehr, Valence band structure of tellurium from shubnikov-de haas experiments, Phys. Stat. Sol. (b) **53**, 635 (1972).
[S9] E. Ivchenko and G. Pikus, Natural optical activity of semiconductors(te), Sov. Phys. Solid State **16**, 1261 (1975).
[S10] H. Stolze, M. Lutz, and P. Grosse, The optical activity of tellurium, Phys. Stat. Sol. (b) **82**, 457 (1977).
[S11] L. Dubinskaya and I. Farbshtein, Natural optical activity and features of the structure of the electronic energy spectrum of tellurium, Sov. Phys. Solid State **20**, 437 (1978).
[S12] T. Furukawa, Y. Shimokawa, K. Kobayashi, and T. Itou, Observation of current-induced bulk magnetization in elemental tellurium, Nature Communications **8**, 954 (2017).
[S13] F. Calavalle, M. Suárez-Rodríguez, B. Martín-García, A. Johansson, D. C. Vaz, H. Yang, I. V. Maznichenko, S. Ostanin, A. Mateo-Alonso, A. Chuvilin, I. Mertig, M. Gobbi, F. Casanova, and L. E. Hueso, Gate-tuneable and chirality-dependent charge-to-spin conversion in tellurium nanowires, Nature Materials **21**, 526 (2022).
[S14] C. Şahin, J. Rou, J. Ma, and D. A. Pesin, Pancharatnam-berry phase and kinetic magnetoelectric effect in trigonal tellurium, Phys. Rev. B **97**, 205206 (2018).
[S15] L. E. Golub, E. L. Ivchenko, and B. Spivak, Electrical magnetochiral current in tellurium, Phys. Rev. B **108**, 245202 (2023).
[S16] M. Sakano, M. Hirayama, T. Takahashi, S. Akebi, M. Nakayama, K. Kuroda, K. Taguchi, T. Yoshikawa, K. Miyamoto, T. Okuda, K. Ono, H. Kumigashira, T. Ideue, Y. Iwasa, N. Mitsuishi, K. Ishizaka, S. Shin, T. Miyake, S. Murakami, T. Sasagawa, and T. Kondo, Radial spin texture in elemental tellurium with chiral crystal structure, Phys. Rev. Lett. **124**, 136404 (2020).
[S17] S. Okumura, R. Tanaka, and D. Hirobe, Chiral orbital texture in nonlinear electrical conduction, Phys. Rev. B **110**, L020407 (2024).
[S18] T. Yoda, T. Yokoyama, and S. Murakami, Current-induced orbital and spin magnetizations in crystals with helical structure, Scientific

Reports **5**, 12024 (2015).

[S19] T. Yoda, T. Yokoyama, and S. Murakami, Orbital edelstein effect as a condensed-matter analog of solenoids, Nano Letters **18**, 916 (2018).

[S20] D. Xiao, M.-C. Chang, and Q. Niu, Berry phase effects on electronic properties, Rev. Mod. Phys. **82**, 1959 (2010).

[S21] M.-C. Chang and Q. Niu, Berry phase, hyperorbits, and the hofstadter spectrum: Semiclassical dynamics in magnetic bloch bands, Phys. Rev. B **53**, 7010 (1996).

[S22] A. Raoux, F. Piéchon, J.-N. Fuchs, and G. Montambaux, Orbital magnetism in coupled-bands models, Phys. Rev. B **91**, 085120 (2015).

[S23] E. Drigo and R. Resta, Chern number and orbital magnetization in ribbons, polymers, and single-layer materials, Phys. Rev. B **101**, 165120 (2020).

[S24] D. Hara, M. S. Bahramy, and S. Murakami, Current-induced orbital magnetization in systems without inversion symmetry, Phys. Rev. B **102**, 184404 (2020).

[S25] K.-W. Kim, H. Jeong, J. Kim, and H. Jin, Vertical transverse transport induced by hidden in-plane berry curvature in two dimensions, Phys. Rev. B **104**, L081114 (2021).

[S26] S. Lee, J. Shin, H. Jeong, and H. Jin, Quantum geometric tensor from real-space twists of chiral chains, Phys. Rev. B **110**, 195139 (2024).

[S27] B. Göbel, L. Schimpf, and I. Mertig, Chirality-induced spin selectivity based on orbital edelstein effect in an analytically solvable model (2025), arXiv:2502.04978.